3D-MICROSTRUCTURING OF SILICON INDUCED BY NANOSECOND PULSED INFRARED FIBER LASER FOR POTENTIAL SOLAR CELL APPLICATIONS

A THESIS SUBMITTED TO
THE GRADUATE SCHOOL OF NATURAL AND APPLIED SCIENCES
OF
MIDDLE EAST TECHNICAL UNIVERSITY

BY

BESNA BÜLBÜL TATBUL

IN PARTIAL FULFILLMENT OF THE REQUIREMENTS
FOR
THE DEGREE OF MASTER OF SCIENCE
IN
PHYSICS

SEPTEMBER 2022

Approval of the thesis:

3D-MICROSTRUCTURING OF SILICON INDUCED BY NANOSECOND PULSED INFRARED FIBER LASER FOR POTENTIAL SOLAR CELL APPLICATIONS

submitted by **BESNA BÜLBÜL TATBUL** in partial fulfillment of the requirements for the degree of **Master of Science in Physics, Middle East Technical University** by,

Prof. Dr. Halil Kalıpçılar
Dean, Graduate School of **Natural and Applied Sciences** ________________

Prof. Dr. Seçkin Kürkcüoğlu
Head of the Department, **Physics** ________________

Assist. Prof. Dr. Ihor Pavlov
Supervisor, **Physics, METU** ________________

Examining Committee Members:

Assoc. Dr. Tahir Çolakoğlu
Physics Eng., Ankara Uni. ________________

Assist. Prof. Dr. Ihor Pavlov
Physics, METU ________________

Assoc. Dr. Emre Yüce
Physics, METU ________________

Date: 02.09.2022

I hereby declare that all information in this document has been obtained and presented in accordance with academic rules and ethical conduct. I also declare that, as required by these rules and conduct, I have fully cited and referenced all material and results that are not original to this work.

Name Last name : Besna Bülbül Tatbul

Signature :

ABSTRACT

3D-MICROSTRUCTURING OF SILICON INDUCED BY NANOSECOND PULSED INFRARED FIBER LASER FOR POTENTIAL SOLAR CELL APPLICATIONS

Bülbül Tatbul, Besna
Master of Science, Physics
Supervisor: Assist. Prof. Dr. Ihor Pavlov

September 2022, 64 pages

Laser-induced three-dimensional (3D) structuring of silicon is a highly desired technology as silicon drives the semiconductor industry with its wide range of applications in solar cells, telecommunications, microelectronics, integrated photonics, etc. Structuring of silicon for such applications is typically performed by lithographic pattern production and pattern transfer via plasma etching, reactive ion etching, or chemical etching. However, conventional lithography methods are limited to the surface of the silicon and do not allow direct fabrication of 3D structures buried deep inside the silicon.

Novel laser-based methods are emerging to fabricate 3D subsurface functional elements in silicon. The 3D structuring of silicon by laser requires high peak intensity, short-pulsed lasers that can induce modification in the silicon by exploiting nonlinear photon absorption. Until recently, laser-induced subsurface modification of the silicon without damaging the surface had been unsuccessful.

In this thesis, highly controlled surface and subsurface modifications are presented in crystalline silicon (c-Si) using a custom-built nanosecond pulsed infrared laser.

To reveal true 3D structures, laser-modified parts are etched in a highly selective chemical solution. Our novel approach is successfully implemented to fabricate 3D microhole arrays inside the c-Si wafer, and 3D micropillar arrays on the surface of the c-Si wafer, for potential applications in transparent solar cells and radial junction photovoltaics, respectively. Since our method does not require mask copying, it offers fewer processing steps than traditional lithographic methods and can be easily adjusted to different applications.

Keywords: 3D laser structuring, silicon subsurface modification, nonlinear photon absorption, transparent silicon, micropillar arrays

ÖZ

POTANSİYEL GÜNEŞ HÜCRESİ UYGULAMALARI İÇİN NANOSANİYE ATIMLI KIZILÖTESİ FİBER LAZER YARDIMIYLA SİLİKONUN ÜÇ BOYUTLU MİKROYAPILANDIRILMASI

Bülbül Tatbul, Besna
Yüksek Lisans, Fizik
Tez Yöneticisi: Dr. Öğr. Üyesi Ihor Pavlov

Eylül 2022, 64 sayfa

Lazer ile silikonun üç boyutlu (3B) yapılandırılması oldukça arzu edilen bir teknolojidir çünkü güneş pilleri, telekomünikasyon, mikroelektronik, entegre fotonik gibi birçok farklı alanda geniş uygulama yelpazesi ile silikon, yarı iletken endüstrisine yön vermektedir. Bu tür uygulamalar için silikonun yapılandırılması genellikle litografik desen üretimi ile başlar ve plazma aşındırma, reaktif iyon aşındırma veya kimyasal aşındırma yoluyla desenin silikona aktarımı ile devam eder. Bununla birlikte, geleneksel litografi yöntemleri silikonun yüzeyiyle sınırlıdır ve silikonun derinliklerine gömülü 3B yapıların doğrudan üretilmesine izin vermez.

Silikonda, 3B yüzey altı işlevsel elemanları üretebilmek için lazer temelli yeni yöntemler geliştirilmektedir. Silikonun lazerle 3B yapılandırılmasında, doğrusal olmayan foton absorpsiyonlarından yararlanarak silikonda modifikasyonu indükleyebilen yüksek ışık yoğunluklu, kısa atımlı lazerlere ihtiyaç duyulur. Yakın zamana kadar, silikon içinde lazerle indüklenen modifikasyon oluşturma yüzeyde hasar bıraktığından başarısız sonuçlanmıştı.

Bu tezde, özel yapım nanosaniye atımlı kızılötesi lazer kullanılarak kristal silikonda (c-Si) oldukça kontrollü oluşturulan yüzey ve yüzey altı modifikasyonlar sunulmaktadır. Asıl 3B yapıları ortaya çıkarmak için, lazerle modifiye edilmiş yerler, oldukça yüksek seçiciliğe sahip bir kimyasal çözelti ile aşındırılmıştır. Yeni yaklaşımızla, c-Si plaka içinde 3B mikro delik dizileri ve c-Si plaka yüzeyinde 3B mikro sütun dizileri sırasıyla saydam güneş pilleri ve radyal bağlantılı fotovoltaiklerde potansiyel kullanımları hedeflenerek başarıyla üretilmiştir. Yöntemimiz maske kopyalama gerektirmediğinden, geleneksel litografik yöntemlere göre daha az işlem adımı sunar ve ayrıca farklı uygulamalara kolayca adapte edilebilir.

Anahtar Kelimeler: 3D lazer yapılandırması, silikon yüzey altı modifikasyonu, doğrusal olmayan foton absorpsiyonu, transparan silikon, mikro sütun dizileri

To the memory of my nephew…

ACKNOWLEDGMENTS

I would like to express my deepest gratitude to my supervisor Dr. Ihor Pavlov for his great support throughout my thesis study. Dr. Pavlov was always available for feedback and guidance on the challenges I faced during my study.

I would like to thank Mona Zolfaghari Borra for her assistance and comments in materials processing and nanosecond laser studies. And also, I thank Arian Goodarzi for his valuable advice and contributions to RSoft simulations.

I want to thank the Center for Solar Energy Research and Applications (GUNAM) for letting me use their facilities and equipment.

I would like to thank my family for their trust and encouragement in my whole life. Finally, I would like to thank Fatih Tatbul for his great understanding and constant support, and appreciate all his sacrifices that enabled me to successfully complete this thesis.

This work was partially funded by TUBITAK BIDEB 2210.

TABLE OF CONTENTS

ABSTRACT v

ÖZ vii

ACKNOWLEDGMENTS x

TABLE OF CONTENTS xi

LIST OF TABLES xiii

LIST OF FIGURES xiv

LIST OF ABBREVIATIONS xvii

CHAPTERS

1 INTRODUCTION 1

1.1 Laser-Induced 3D Modification in Silicon 3

2 THEORETICAL BASIS 7

2.1 Laser-Material Interaction 7

2.1.1 High-Intensity Laser–Material Interaction in Transparent Medium ... 7

2.2 Silicon Etching Methods 12

2.2.1 Metal-Assisted Chemical Etching 14

2.2.2 Selective Etching of Laser-modified Region with Cu-ACE 17

3 3D MICROPILLAR ARRAYS FABRICATION ON SILICON WAFER 21

3.1 Introduction 21

3.2 Experimental 23

3.2.1 Laser Setup 23

3.2.2 Laser Surface Processing 25

3.2.3 Micropillar Fabrication Procedure 26

3.2.4 SIMS Analysis 40

4 FABRICATION OF NEUTRAL-COLORED TRANSPARENT SILICON WAFER VIA 3D MICROHOLE ARRAYS 41

4.1 Introduction 41

4.2 Design Criteria for Microhole-based Transparent c-Si Substrate 42

4.2.1 Spacing Criterion 43

4.2.2 Hole Diameter Criterion 44

4.3 Experimental 45

4.3.1 Laser Subsurface Processing 45

4.3.2 Fabrication Procedure of Microhole-based Transparent c-Si Substrate 46

5 CONCLUSION 57

REFERENCES 59

LIST OF TABLES

TABLES

Table 3.1 Weighted reflection of non-etched, 10 min. etched, and 15 min. etched samples with 20 µm step-sized pillars. (Process area: 5 mm × 5 mm). 39

Table 4.1 Number of holes and laser process times for hexagonal arrayed microholes with different periods. (Process area: 8 mm × 8 mm).. 46

Table 4.2 Filling fraction and AVT values at different hole diameters and spacings. 52

LIST OF FIGURES

FIGURES

Figure 2.1 Timescale of physical phenomena during ultrashort pulse laser-material interaction. 11
Figure 2.2 Schematized MACE process for a Si substrate immersed in $AgNO_3$/HF aqueous solution. (a) Formation of solid Ag nucleation on Si substrate. (b) Growing of Ag nucleation into Ag nanoparticles and induced local oxidation of Si. (c) Dissolution of oxidized Si via HF and sinking of catalyst into Si substrate. 15
Figure 3.1 Schematic representation of light absorption and photo-generated carrier separation in a planar (a) and radial (b) junction solar cell. (c) Absorption spectra of planar Si and microwire arrays with different lengths. (Each microwire has a diameter of 2 μm and spacing between the wires is 2μm.) 22
Figure 3.2 Schematic of custom-built 1550 nm, ns-pulsed laser setup. MM, multimode; MPC, multiple-port pump-signal combiner; WDM, wavelength division multiplexer; QWP, quarter-wave plate; HWP, half-wave plate; PBS, polarizing beam splitter. 24
Figure 3.3 Photographs of ns-laser setup. 24
Figure 3.4 Plasma generation on Si surface during laser processing. 25
Figure 3.5 (a) Schematic representation of raster scan on Si surface. (b) SEM image of pillar structures formed on c-Si wafer after raster scan. 25
Figure 3.6 ns-laser structured c-Si sample sets each with 20 μm, 30 μm, 40 μm, 50 μm, and 60 μm laser step sizes. 27
Figure 3.7 SEM images of 10 min. etched sample set showing Si micropillar arrays at 1000X magnification. 28
Figure 3.8 SEM images of 20 min. etched sample set showing Si micropillar arrays at 1000X magnification. 29
Figure 3.9 SEM images of 30 min. etched sample set showing Si micropillar arrays at 1000X magnification. 30

Figure 3.10 SEM images of 40 min. etched sample set showing Si micropillar arrays at 1000X magnification.. 31
Figure 3.11 SEM images of 50 min. etched sample set showing Si micropillar arrays at 1000X magnification.. 32
Figure 3.12 SEM images of 60 min. etched sample set showing Si micropillar arrays at 1000X magnification.. 33
Figure 3.13 45^0 tilted SEM images of 60 min. etched sample showing Si micropillar depths at 1000X magnification for (a) 50 µm and (b) 60 µm step sizes................ 34
Figure 3.14 Micropillar width variation with increasing etching time. 34
Figure 3.15 Reflectance spectrums of micropillar structures. (Each graph shows the reflectance spectra for the same laser step size etched between 10 and 60 min.)... 35
Figure 3.16 Weighted reflectance for different step-sized pillars etched between 10 and 60 min... 37
Figure 3.17 45^0 tilted SEM images of 10 min. etched sample showing 3D periodic Si micropillar structures with 20 µm step size. (Process area: 2 mm × 2 mm). 37
Figure 3.18 SEM images of 10 min. etched sample with 20 µm step size. (Process area: 5 mm × 5 mm). 38
Figure 3.19 SEM images of 15 min. etched sample with 20 µm step size. (Process area: 5 mm × 5 mm). 38
Figure 3.20 Reflection spectra of non-etched, 10 min. etched, and 15 min. etched samples with 20 µm step-sized pillars. (Process area: 5 mm × 5 mm). 38
Figure 3.21 SIMS profile on micropillar surface 40
Figure 4.1 Illustration of minumum resolvable spacing between holes distinguishable by human eye at distance L from c-Si substrate. 43
Figure 4.2 Visible light interaction with periodic holes having diameters (a) 0.5 µm, (b) 5 µm and (c) 20 µm simulated in RSoft Photonic Device Tools....................... 44
Figure 4.3 Schematic representation of subsurface processing for hexagonal arrayed microholes in c-Si substrate. 45
Figure 4.4 Optical microscope images showing diameters of laser-modified regions for (a) 60 µm (b) 70 µm and (c) 80 µm periods. 47

Figure 4.5 SEM images of etched Si microhole arrays having 60 μm period. (a) Top surface image at 100X magnification, (b) 75^0 tilted image at 1000X magnification, (c) top surface image at 1000X magnification, (d) 75^0 tilted cross-section image at 100X magnification. 48
Figure 4.6 SEM images of etched Si microhole arrays having 70 μm period. (a) Top surface image at 200X magnification, (b) 75^0 tilted image at 1000X magnification, (c) top surface image at 1000X magnification, (d) 75^0 tilted cross-section image at 500X magnification. 49
Figure 4.7 SEM images of etched Si microhole arrays having 80 μm period. (a) Top surface image at 200X magnification, (b) 75^0 tilted image at 1000X magnification, (c) top surface image at 1000X magnification, (d) 75^0 tilted cross-section image at 500X magnification 50
Figure 4.8 (a) Transmittance spectra of hexagonal arrayed c-Si microholes with different periods. (b) Corresponding neutral-colored transparent c-Si substrate where each transparent region having a different hole period as indicated in upper photograph. 51
Figure 4.9 CIE 1931 chromaticity diagram showing color coordinates of the transparent regions on the c-Si substrate having different hole periods. (Illuminant D65 represents color coordinates of standard daylight illuminant.) 53
Figure 4.10 (a) Optical microscope images of laser-modified square arrayed region. (b) Top view SEM image of etched Si microhole arrays having 80 μm period at 1000X magnification. (c) Cross-section SEM image of etched and polished Si microhole arrays at 800X magnification. 54
Figure 4.11 (a) Transmittance spectra of square arrayed c-Si microholes with 80 μm period. (b) Corresponding neutral-colored transparent c-Si substrate. (Upper left photo is of laser-structured c-Si substrate taken before etching.) 55

LIST OF ABBREVIATIONS

ABBREVIATIONS	
3D	Three dimensional
c-Si	Crystalline silicon
MACE	Metal assisted chemical etching
Cu-ACE	Copper assisted chemical etching
PV	Photovoltaic
TPV	Transparent photovoltaic
AVT	Average visible transmittance

CHAPTER 1

INTRODUCTION

The theoretical basis of laser technology was first described by Albert Einstein in 1917 [1]. He proposed the concept of "stimulated emission", which makes lasers possible. After several failed attempts, the first working device for light amplification by stimulated emission of radiation (laser) was constructed in 1960 at Hughes Research Laboratories by Theodore H. Maiman [2]. Since then, many different types of lasers (e.g., solid-state lasers, gas lasers, liquid lasers, and semiconductor lasers) were developed with shorter pulses and higher peak powers. Unlike ordinary light, laser light has unique characteristics such as coherence, monochromaticity, and directionality. These contribute to the exceptional focusability of the laser beam, which enables the high intensities up to 10^{21} W/cm^2 that are capable of vaporizing any material or even starting nuclear fusion [3]. Today, laser technology is applied in many different areas such as manufacturing industry, communication, medicine, military, scientific research, etc. because of the unique characteristics of laser light.

Depending upon the desired application, lasers can be operated in either pulsed mode or continuous wave mode. In continuous wave operation, laser output power is nearly constant with time, whereas in pulsed operation, the output power emerges as a series of brief pulses at a certain duration and repetition rate. Since pulsed lasers emit optical energy in a very short time, the pulsed laser can reach much higher peak power values than a continuous wave laser with the same amount of energy. Due to its high peak power, the pulsed lasers with a typical pulse duration ranging from nanosecond (10^{-9} s) to femtosecond (10^{-15} s) are ideal tools for high precision micro/nano machining of various materials. The small pulse duration results in small

heat affected zone and controlled material processing owing to the short interaction time between the laser and the material [4, 5].

Laser-material interaction and induced modifications primarily depend on laser intensity, optical properties of the material, laser wavelength, and interaction time. When a material is irradiated by a laser beam, a part of the photons is reflected, absorbed, and/or transmitted. The absorbed laser energy can cause heating, melting, evaporation, plasma formation, etc., depending on the absorbed laser power density and the interaction time. Linear single-photon absorption is a typical form of energy absorption [6]. If laser photon energy, hv more than the bandgap of the material, an electron can be directly excited from the valence band to the conduction band through the linear absorption of a photon. In the case of photons with energy smaller than the bandgap, the material is transparent for that wavelength because linear absorption is no longer allowed. However, when a higher intensity laser beam is tightly focused into the material, the electron can be excited to the conduction band by multiphoton absorption even though the photon energy is below the bandgap energy. After excitation of the electrons, thermal diffusion of the electrons occurs and energy is transferred to the lattice (ions) through electron-phonon coupling. This results in a rapid local increase of temperatures at the interaction region. The evolution of the temperature will determine the final material modification or damage in the interaction volume [7].

The high peak intensity of short-pulsed laser enables 3D material modification through nonlinear absorption if the laser energy is accurately delivered into focal volume. By focusing the laser beam at various depths in the material, both surface and subsurface processing of the material is possible with this approach. Furthermore, within the research on laser-material interaction, high-intensity lasers are of growing interest for fabricating 3D modifications in silicon [8]. This thesis is focused on the application of high-intensity short-pulsed lasers using the principle of nonlinear absorption for both surface and subsurface modification of silicon.

1.1 Laser-Induced 3D Modification in Silicon

Conventional lithography methods do not enable the direct fabrication of functional elements buried deep inside material. However, laser-based processing has the ability to directly produce 3D structures without a mask deep inside materials by eliminating the time-consuming and expensive multistep approach of conventional lithographic methods. Fabrication in 3D can be accomplished by tightly focusing the high-power short-pulsed laser into the bulk of material that induces nonlinear processes such as multiphoton and avalanche ionization resulting in permanent material modification within the focal volume [9]. Laser-induced subsurface modifications have been successfully implemented for the fabrication of optical elements such as waveguides, interconnects, and resonators inside transparent dielectric materials (e.g. glasses, polymers, crystals) [10]. However, laser-based 3D machining of semiconductors is a relatively new topic. And, efforts to fabricate functional optical elements inside the bulk of silicon through laser-induced modifications had been unsuccessful until recently. This is related to the physical properties of silicon, such as its infrared transparency, high refractive index ($n = 3.47$), high thermal diffusivity, etc., which set some limits on the laser system to be used [8]. Therefore, machining of the silicon requires laser systems with higher repetition rates and higher pulse energies compared to dielectrics.

Current manufacturing methods for silicon, notably photolithography, enable planar patterns on wafer surfaces. The silicon-on-insulator (SOI) method is widely used to form 3D structures in the silicon in a layer-by-layer fashion [11]. Although the SOI method is well defined, its planar character does not allow complex structures, also, the presence of multiple steps increases defects and thus degrades the performance of the device.

Forming laser-induced controlled structures inside silicon will be revolutionary since, silicon with its unique electrical properties, is the backbone material of the semiconductor industry. It is non-toxic and the second most abundant element in the world and has countless applications including solar cells, telecommunications,

micro/nanoelectronics, etc. Therefore, laser-induced subsurface modification of silicon is a highly desired technology and can also lead to the development of novel electronic/photonic devices. However, the physical mechanisms underlying the laser-induced subsurface modification of silicon are not entirely understood yet due to the complex nature of the laser-material interaction.

Early demonstrations of direct-laser writing for silicon focused on the fabrication of surface structures like super-wicking [12] and black silicon [13] used in applications such as microfluidics, photovoltaics, etc. So far, most of the efforts to create laser-induced subsurface modifications in silicon have been conducted with ultrafast lasers. The first attempt was made by Nejadmalayeri et al., who demonstrated the creation of optical waveguides using a femtosecond laser [14]. However, regardless of the depth of focus within the silicon wafer, the waveguides could only be produced very close to the surface. Additional efforts were not successful in creating truly subsurface modifications in silicon without damaging the surface because of absorption or strong plasma-shielding effects [15]. Even using extremely high pulse energies up to 90 μJ, the subsurface structures were not observed [16]. Later, Tokel, Pavlov, et al. reported the first laser-induced modifications deep inside the silicon without damaging the wafer surface using nanosecond pulsed infrared lasers in 2014 [17, 18]. Following that, several studies based on similar approaches were reported both with nanosecond and femtosecond laser pulses [19, 20].

The widely used laser for silicon processing has been the diode-pumped solid-state laser with 355 nm or 266 nm wavelength [21]. On the other hand, recent advances in fiber lasers have opened up new opportunities in the applications of laser-induced material modification. And, fiber lasers are increasingly employed in silicon modification due to their improved processing capabilities. In these lasers, the gain medium is an optical fiber doped with rare-earth elements such as erbium, ytterbium, and neodymium, and is pumped mostly by semiconductor diode lasers. The fiber lasers provide high powers without damaging the optical fiber and excellent beam quality which enhances the quality of machining. The large surface area of the fiber enables the dissipation of excess heat along the entire fiber length. In addition, they

are low-cost, long-term stable systems and offer simple operation due to their compact size and high tolerance for misalignment [18, 22].

In this thesis, a maskless laser-induced method to generate highly controllable 3D modifications in the silicon wafer is demonstrated without thermally triggered detrimental effects, i.e., microcracking and surface damage. We use a custom-developed nanosecond-pulsed erbium-ytterbium co-doped fiber laser that produces pulses around 6 ns and operates at 1550 nm wavelength. Since, the silicon is transparent to the 1550 nm wavelength, by tightly focusing the high-power laser, we induce the silicon modification by absorbing light via nonlinear processes. And, in the laser-modified parts, a change in refractive index occurs, which can allow the production of various photonic components in the silicon. On the other hand, in order to truly achieve 3D structures, these laser-modified parts need to be selectively etched. Therefore, a highly selective chemical etching solution is applied to reveal the desired 3D structures by removing essentially laser-modified zones from the c-Si wafer. By utilizing these novel approaches, periodic arrays of 3D microholes inside the c-Si wafer, as well as periodic arrays of 3D micropillars on the surface of the c-Si wafer, are fabricated for potential applications in transparent solar cells and radial junction photovoltaics, respectively. The laser-induced silicon processing method demonstrated here is maskless, rapid, low-cost, and easily scalable to large areas. It offers new possibilities to the currently used silicon machining methods, and the fabrication of various functional structures in silicon such as microfluidic channels, microresonators, multilayered chips, information storage, micro-electro-mechanical systems, etc. is possible [23].

CHAPTER 2

THEORETICAL BASIS

2.1 Laser-Material Interaction

Upon irradiating a material with a laser, if the incident photon energy is equal to or higher than the band gap of the material, the electrons in the material absorb the laser energy and are excited to the conduction band. This is called one photon or linear absorption and the absorption probability scales linearly with the laser intensity. The one-photon absorption of a laser beam propagating through a linearly absorbing medium is characterized by an absorption coefficient α, such that

$$\frac{\partial I}{\partial z} = -\alpha I \tag{2.1}$$

where, I is the intensity of the laser, and z is the absorption depth [24].

When the photon energy is smaller than the band gap energy, linear absorption is not allowed, and the material is said to be transparent at that irradiating wavelength. However, if the laser intensity is sufficiently high, the nonlinear response of the material gives rise to multiphoton ionization (or multiphoton absorption) and subsequent avalanche ionization [10]. Silicon having a bandgap of 1.12 eV is transparent to infrared spectrum with wavelengths approximately above 1.1 μm. Thus, to induce modification in the silicon, the nonlinear interaction regime is required which is achievable at high intensities.

2.1.1 High-Intensity Laser–Material Interaction in Transparent Medium

The propagation of a laser pulse in a transparent material can be described by Equation 2.2,

$$\nabla^2 E - \frac{1}{c^2}\frac{\partial^2 E}{\partial t^2} = \mu_0 \frac{\partial^2 P}{\partial t^2} \quad (2.2)$$

where c is the speed of light in vacuum and μ_0 is the permeability of free space [25]. This equation is known as the wave equation derived from Maxwell's equations. The applied electromagnetic wave tends to separate positive and negative charges in the medium, thereby inducing polarization P(t) of the material. The induced polarization includes both linear effects like absorption, refraction, diffraction and nonlinear effects such as self-focusing, multiphoton absorption, etc.

Under high-intensity laser, the induced polarization P(t) is expressed as a power (Taylor) series of the applied electric field E(t), in the form [26, 27],

$$P(t) = \varepsilon_0 \chi^1 E(t) + \varepsilon_0 \chi^2 E^2(t) + \varepsilon_0 \chi^3 E^3(t) + \cdots \quad (2.3)$$

where $\chi^{(n)}$ are n-th order electrical susceptibilities of the material and ε_0 is the permittivity of free space. χ^1 defines the linear interaction, while the higher order terms represent the nonlinear response of the material. Silicon is a centrosymmetric media, that is, its crystal structure displays inversion symmetry [28]. In the centrosymmetric media, all the even-order nonlinear susceptibility terms vanish, hence only the odd-order susceptibility terms can contribute to the induced polarization in silicon atoms.

Transferring Equation 2.3 into frequency domain, the induced polarization and the nonlinear effects associated with each of the susceptibility order can be described in terms of frequency components. Further, the general form of Equation 2.1 that includes multiphoton absorptions can be expressed as [24],

$$\frac{\partial I}{\partial z} = -\alpha I - \beta I^2 - \gamma I^3 \quad (2.4)$$

Here, α, β, γ are the first, second, and third order photon absorption coefficients, which determine the magnitude of the multiphoton absorption. The first term represents the linear absorption while all terms of order >1 are referred to as multiphoton absorption.

A medium is considered transparent when its linear absorption coefficient is negligible. The linear absorption coefficient of silicon at 1550 nm wavelength is ~10^{-8} cm^{-1} thus the first term in Equation 1.4 is ignored. This means that the two-photon absorption is the dominant process at high intensities and scales as the square of the laser intensity, I^2. In silicon at 1550 nm wavelength, the two-photon absorption coefficient is reported as ~0.45 cm/GW [29].

Multiphoton absorption depends on the simultaneous absorption of two or more photons, which excites an electron to the conduction band. And, since it is direct ionization, there is no certain threshold intensity for activation. Multiphoton ionization generates the initial (seed) electron density, which is then grown by the avalanche ionization. The multiphoton ionization rate (the probability of ionization per atom per second) can be given as [30]

$$\omega_{mpi} \approx \omega n_{ph}^{3/2} \left(\frac{\varepsilon_{osc}}{2\Delta_{gap}} \right)^{n_{ph}}, \qquad n_{ph} = \frac{\Delta_{gap}}{\hbar\omega} \tag{2.5}$$

Here, ω is the the laser frequency, ε_{osc} is the electron oscillation energy, Δ_{gap} is the electronic band gap and n_{ph} is the number of photons that an electron must absorb to be promoted from valence to the conduction band. As seen in equation, the probability is directly proportional to the oscillation energy of the electron thus the laser intensity is an important parameter to initiate the multiphoton ionization.

Unlike multiphoton ionization, direct photon absorption by electrons in the valence band is negligible in avalanche ionization. A few (seed) electrons in the conduction band oscillate in the electromagnetic field of the laser and can gain energy by multiple electron-phonon (lattice) collisions. Electrons accelerated to the energy higher than the bandgap ($\varepsilon_{osc}>\Delta_{gap}$) can collide with the valence band electrons and transfer sufficient energy to excite them into the conduction band. Thus, an avalanche of ionization events is created in the material. The probability of impact ionization per unit time can be estimated as follows,

$$\omega_{imp} \approx 2\frac{\mathcal{E}_{osc}}{\Delta_{gap}}\frac{\omega^2 v_{eff}}{(v_{eff}^2 + \omega^2)} \tag{2.6}$$

where υ_{eff} is the effective electron–lattice collision rate [30].

For impact ionization to occur, initial electron density, n_0, should be sufficiently high. The excited electron density, n_e, generated by avalanche process is expressed as,

$$n_e(t) = n_0 2^{\omega_{imp} t} \tag{2.7}$$

When the excited electron density (n_e) reaches a critical density level (n_c), i.e., $n_e = n_c$, the material undergoes optical breakdown. The critical density depending the frequency of the incident light is given as

$$n_c = \frac{m_e \omega^2}{4\pi e^2} \tag{2.8}$$

where m_e and e are the electron mass and electron charge, respectively [31].

Multiphoton absorption and avalanche ionization are two primary mechanisms that transform the material into plasma. During ionization processes in the transparent medium, other nonlinear mechanisms can also occur because of the high-intensity laser beam. In terms of laser machining, self-focusing and plasma defocusing are the most important nonlinear mechanisms that cause significant distortion of the incident laser beam. The self-focusing effect usually occurs when the refractive index at the center of the beam is higher than the rest of the interacting region, causing the beam to collapse on itself. The beam collapse can be arrested by plasma defocusing since the presence of free carriers reduces the refractive index at the center of the beam. The beam can continuously switch between self-focusing and plasma defocusing, which keeps the beam confined as it propagates over long distances.

The process duration for multiphoton absorption and avalanche ionization is around 10^{-14} - 10^{-11} seconds. The relative contribution of both ionization processes varies at different pulse durations, intensities, wavelengths, and for different material

properties. The excited electrons in the conduction band transfer energies among themselves through carrier-carrier scattering, which typically occurs in the order of 10 to 100 fs time duration. Then, the excess energy of the electrons is transferred to the lattice through carrier-phonon scattering on a time duration of ~10 ps. For ns-pulsed laser, all these events take place within the pulse duration, thus the energy transferred from the electrons to the lattice cannot be limited to the focal spot diameter; the excited lattice phonons spread energy surroundings of the laser focal spot through thermal diffusion. Figure 2.1 illustrates general timescales of relevant physical events [10].

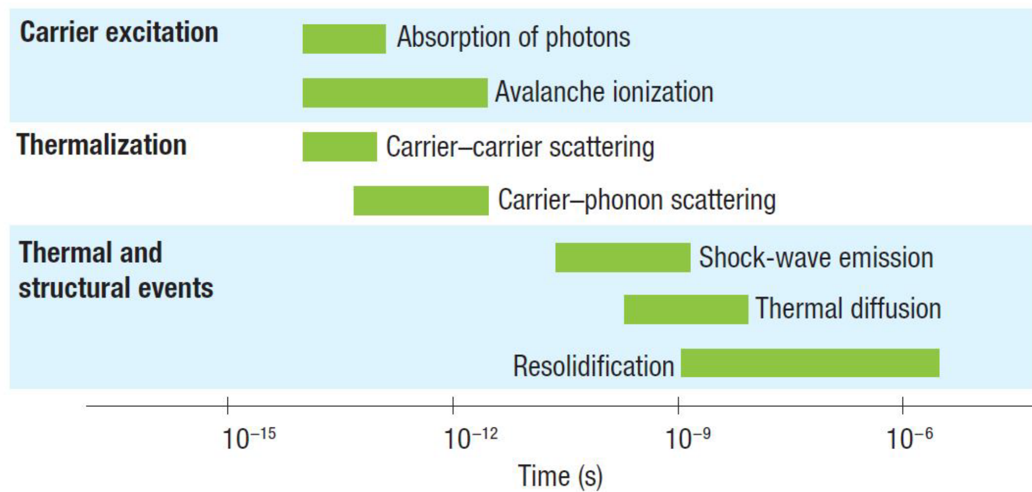

Figure 2.1 Timescale of physical phenomena during ultrashort pulse laser-material interaction.

At high laser intensities around 10 GW/cm^2 generated by ns pulses, the valence band electrons are excited into the conduction band through nonlinear photoionization processes [32]. And, the ionization of material produces free-electron plasma cloud, which increases absorption of the incident laser. This is accompanied by the creation of a high energy density at the focal volume that exerts mechanical stresses to the lattice. The subsequent modification or damage can be precisely controlled due to the high localization of intense energy. Therefore, fabrication of various 3D structures within transparent materials is possible with high-intensity lasers.

2.2 Silicon Etching Methods

There are many different etching methods used in the fabrication of silicon micro and nanostructures, which can be classified into two main categories, namely dry etching and wet etching. As being a top top-down approach, prior to the etching, a photoresist material is coated on the silicon substrate, and then a mask with the desired pattern is transferred onto the photoresist by a lithographic process. Once the mask pattern is defined, the silicon substrate not protected by the mask can be removed using either wet or dry etching methods.

The most commonly used silicon etching method is deep reactive ion etching (DRIE), which is one of the dry etching methods based on the Bosch process [33]. The DRIE-Bosch process consists of alternating etch and passivation cycles in a vacuum chamber. Each successive cycle only lasts a few seconds, and high aspect ratio micropillars or microholes can be produced by repeating the cycles as many times as needed, regardless of the crystallographic orientation of the silicon. In general, SF_6 gas is used for silicon etching and a fluorocarbon gas (e.g. C_4F_8) is used for deposition of a passivation layer. The silicon etching with fluorine atoms formed by dissociation of SF_6 gas in plasma is intrinsically isotropic. However, during the etching phase, directional ion bombardment from the plasma sputters away the passivation layer at the bottom and at the top of the photoresist, but the passivation layer at the sidewalls remains so that the silicon bottom region is anisotropically etched by fluorine atoms [34]. Because of the cyclic steps in the Bosch process, a scallop shape is formed on the sidewalls. These scallops and plasma-induced surface damage degrade the performance of the device by reducing the lifetime of minority carriers. Also, the process requires specialized high cost vacuum-based equipment.

Wet etching, unlike dry etching, does not require high-cost vacuum-based instruments; it can be simply carried out in a fume hood within a standard laboratory. Among various wet etching methods, KOH is one of the most commonly used etchant for single c-Si due to its high degree of anisotropic etching property, i.e. (111) planes are etched much slower than (100) and (110) planes. However, straight

pillar or hole structures with a high aspect ratio cannot be produced using conventional wet etching methods.

As an alternative wet etch approach to form high aspect ratio silicon micro and nanostructures, metal-assisted chemical etching (MACE) has gained great interest in recent years for several reasons. First, MACE is a low-cost process based on a simple redox system that enables to produce high-quality structures typically at room temperature. Thus, metal contamination into silicon caused by high temperatures is prevented. The method eliminates plasma-induced surface damage or scallops caused by high-energy ions which is common in the dry etching processes. Second, very high aspect ratio, vertical structures can be produced since the MACE is intrinsically anisotropic and the main factor determining growth direction is wafer crystal orientation. Due to relatively low bond energy, the Si atom on the (100) surface plane is the most easily removed, and the Si etching proceeds preferably along the crystallographic <100> direction that leads to the formation of vertical structures on the Si (100) substrate. Third, various structures with different cross-sectional shapes, diameters, and lengths can be readily achieved by adjusting etching parameters (e.g., initial geometry of catalytic metal species, concentration, etching duration, temperature, substrate resistivity, and crystal orientation). Typically, the etching direction depends on the crystallographic orientation of the wafer but this can be overcome by adjusting the etching parameters. This allows control of the crystal orientation of the starting wafer as well as wafer type and doping level. Furthermore, the MACE can be applied to single-crystalline Si, multi-crystalline Si, or amorphous Si, as well as other different materials, such as GaAs and GaN. Finally, the MACE is compatible with existing nano/microfabrication technology and has the potential for large-scale industrial production owing to its simple experimental setup, large-area process, and fast etching rate [35-38].

Among various methods, the MACE is the most cost-effective process for silicon etching, thus, it is applied in this thesis study to remove laser-modified parts from the c-Si wafer to reveal the desired 3D structures. In the following section, a fundamental description of the MACE is given.

2.2.1 Metal-Assisted Chemical Etching

MACE is a typical electroless galvanic process driven by a series of reduction-oxidation (redox) reactions at the cathode (solution-catalyst interface) and anode (catalyst-substrate interface), respectively [38, 39]. In this fabrication method, a metallic catalyst (e.g., Au, Ag, Pt, Pd, Fe, and Ni) is used to accelerate the etching process in a solution that mainly contains an oxidant, an acid, and sometimes a diluent or surfactant [40]. At the cathode, the metal catalyzes the reduction of the oxidant agents, hence forming holes that are injected into the substrate interfacing with the metal. Only the substrate in contact with the metal becomes ionized. Therefore, at the anode, the substrate is selectively oxidized and then dissolved within the MACE solution. Continuously repeating such redox reactions and dissolution cycles under regulated conditions enables for rapid anisotropic etching of the substrate, thereby leading to the formation of various surface morphologies such as pillars, holes, cones, etc [41, 42].

The MACE method was first presented in detail by Li and Bohn in 2000. They demonstrated that a noble metal on the surface of a c-Si substrate catalyzed the etching of Si in a mixed solution consisting of HF, H_2O_2, and organic solvents, generating straight pores or columns [43]. Then, this etching method attracted a wider field of interest and different approaches were derived from their method.

Typically, the MACE is classified into one-step (direct etching) and two-step (depositing and etching) MACE. In the one-step MACE, the Si etching takes place in an aqueous solution that mostly includes HF and metallic salt catalyst. Whereas in the two-step MACE, the catalyst is deposited on the Si substrate prior to the etching by sputtering, thermal evaporation, beam evaporation, etc., then the metal-deposited substrate is immersed in the etching solution [44].

One-step MACE: $AgNO_3$/HF is a commonly used one-step MACE system for Si etching [45]. And, the main processes of the system are schematically shown in Figure 2.3. Ag^+ ions formed in the solution have stronger electronegativity than the

Si, thus Ag^+ ions attract electrons from the Si and are reduced into solid Ag atoms. Gradually, Ag atoms grow into Ag nanoparticles and are deposited on the Si surface. Concurrently, due to hole injection (from Ag^+ ions), the Si underneath the deposited Ag particles is selectively oxidized and the resultant SiO_2 is etched by HF. The proposed cathodic reaction for Ag^+ reduction and anodic reaction for Si oxidation and dissolution are given as,

Cathode: $$Ag^+ \rightarrow Ag(s) + h^+ \quad (2.9)$$

Anode: $$Si(s) + 2H_2O + 4h^+ \rightarrow SiO_2 + 4H^+ \quad (2.10)$$

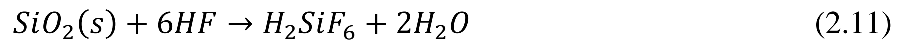

$$SiO_2(s) + 6HF \rightarrow H_2SiF_6 + 2H_2O \quad (2.11)$$

As the oxide layer is dissolved by HF, the Ag particles sink into the substrate, causing anisotropic etching of the Si. The etching continues as long as the HF reaches the Ag-Si interface. If the size of the Ag particles increases and eventually covers the entire Si surface, the etching will stop.

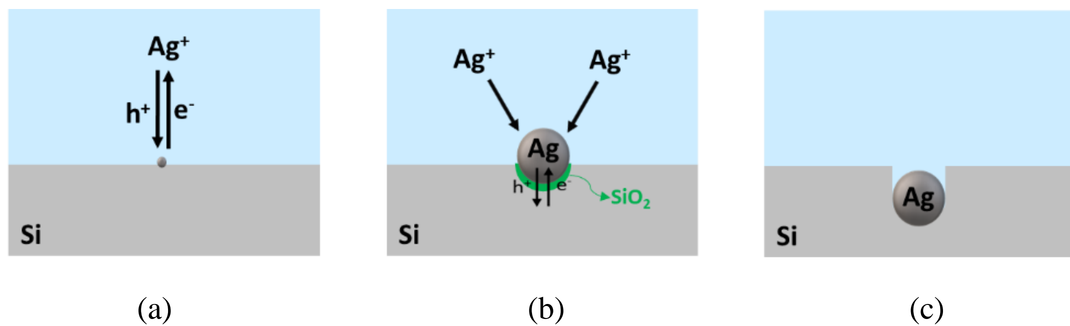

Figure 2.2 Schematized MACE process for a Si substrate immersed in $AgNO_3$/HF aqueous solution. (a) Formation of solid Ag nucleation on Si substrate. (b) Growing of Ag nucleation into Ag nanoparticles and induced local oxidation of Si. (c) Dissolution of oxidized Si via HF and sinking of catalyst into Si substrate.

Aside from $AgNO_3$, there are other metal-based oxidants such as $KAuCl_4$, K_2PtCl_6 and Cu $(NO_3)^2$ that can be used to drive the Si etching [35]. By mixing HF with these oxidants, Au, Pt and Cu particles can be electrolessly deposited on the Si surface.

Two-step MACE: First, a metal film of Ag, Au, Pt, Pd, etc. is deposited on the Si substrate as a catalyst, with films typically being patterned to produce desired

structures. Then, the metal-deposited substrate is immersed in a mixed etchant that contains HF and an appropriate oxidant such as H_2O_2 [38]. As represented by equation (2.12), at the cathode, the reduction of H_2O_2 on the surface of the metal catalyst generates holes that are injected into the Si substrate underneath the metal. The presence of the metal catalyst promotes the reduction of H_2O_2, thereby improving the etching rate by accelerating hole injection into the valence band of the Si. At the anode, the Si surrounding the metal catalyst is selectively oxidized and dissolved. For the dissolution of Si, a variety of reaction mechanisms have been proposed, which can be mainly divided into three groups: tetravalent dissolution, divalent dissolution, and oxide formation and dissolution [35]. Chartier et al. [46] suggested a mixed reaction composed of tetravalent and divalent dissolution for the direct dissolution of Si as shown in equation (2.13).

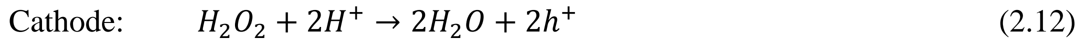

Cathode: $$H_2O_2 + 2H^+ \rightarrow 2H_2O + 2h^+ \quad (2.12)$$

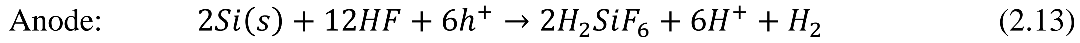

Anode: $$2Si(s) + 12HF + 6h^+ \rightarrow 2H_2SiF_6 + 6H^+ + H_2 \quad (2.13)$$

$$SiO_2 + 6HF \rightarrow H_2SiF_6 + 2H_2O \quad (2.14)$$

Since the redox reactions are localized underneath the metal catalyst, the etching of Si in contact with the metal is much faster. Koynov et al. showed that the etching rate without catalyst was very low (~1 nm/min), whereas this rate was significantly increased with the addition of Au catalyst; 250 nm deep structures were produced in 50–90 seconds [47]. Moreover, as the metal catalyst travels into the cavity formed by the etched Si, the morphologies of the etched Si surface are ultimately defined by the shape and size of the catalyst.

The exact mechanisms of the MACE are not yet known because of challenges in direct in-situ exploration. However, it has been found that various parameters can affect the etching rate and/or morphologies of resultant structures such as catalyst type, etching solution concentration, etching duration, temperature, illumination, doping type, doping level, etc [48].

In the MACE method, the metal catalyst is usually selected from Au, Ag, and Pt because of their stability and fast etching rate in HF/ H_2O_2 etching solution. However, they are expensive and also detrimental to the performance of the device because of the high diffusivity of these precious metals in Si [41]. A lower-cost alternative metal catalyst such as Cu can be used in the MACE despite its weak catalytic activity. In addition, Cu is substantially less damaging to Si devices than Au and Ag [48-50]. In spite of these benefits, copper is not a commonly utilized catalyst in the MACE.

The MACE has been widely applied for the fabrication of Si nanostructures, but there have been relatively few attempts for the microfabrication of Si. In this thesis, Cu is used as the catalyst in the MACE process. And 3D Si microstructures are produced by selectively removing the laser-modified silicon with Cu-assisted chemical etching (Cu-ACE). The Cu-assisted etching is based on the one-step MACE, but we combine it with direct laser machining to achieve regular and predictable arrays of micropillars and microholes.

2.2.2 Selective Etching of Laser-modified Region with Cu-ACE

Laser processing allows generating intentional modification (defect) in predefined regions of the silicon. In order to reveal 3D structures out of the silicon bulk, highly selective etching of the laser-processed region is required. The use of nanosecond pulsed lasers to create 3D structures in silicon is a novel technique. Accordingly, there is no proven method for selectively removing the laser-modified regions without causing damage to the unprocessed regions of the silicon.

For highly selective etching on the laser-modified regions of the silicon wafer, we adapted the MEMC (Monsanto Electronic Materials Company) etching [51] to our study. The MEMC etching is a copper (II) nitrate-based etchant that is suitable for both n- and p-type silicon wafer etching. The etchant exhibits a long lifetime without

overheating solution, and can be applied at room temperature. Additionally, it does not include any harmful metallic species or produce any dangerous gases.

The MEMC etch is a mixture of $Cu(NO_3)_2$, HF, HNO_3, CH_3COOH in DI H_2O. In 100 ml of etching solution, a composition of HF:HNO_3:CH_3COOH:H_2O – 36:25:18:21 (vol%) are used with 1 g of $Cu(NO_3)_2$. This etching recipe provides smooth surfaces at a high etch rate with insignificant etching of the unprocessed silicon regions. The $Cu(NO_3)_2$ is catalytic metal salt that accelerates the reaction at specific defect sites. In the mixture, both acetic acid and water serve as diluents. Acetic acid also serves as a surfactant resulting in smoother surface structures and less foaming during etching.

The general etching mechanism of Cu-ACE is similar to typical one-step MACE. As with other metal catalysts, the Cu is more electronegative than the Si (1.9 eV versus 1.8 eV, respectively) [52], enabling the removal of electrons from the Si. During the Cu-ACE, generation of H_2 gas was observed, and the light blue color of the solution changed into green, suggesting the presence of nitric oxide (NO) [51]. Thus, we predict anodic and cathodic reactions as follows:

Cathode: $Cu^{2+} \rightarrow Cu(s) + 2h^+$ (2.15)

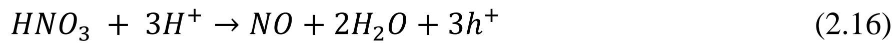

$HNO_3 + 3H^+ \rightarrow NO + 2H_2O + 3h^+$ (2.16)

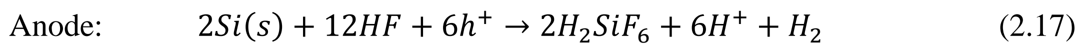

Anode: $2Si(s) + 12HF + 6h^+ \rightarrow 2H_2SiF_6 + 6H^+ + H_2$ (2.17)

$SiO_2 + 6HF \rightarrow H_2SiF_6 + 2H_2O$ (2.18)

When the Si wafer is immersed into the etchant, Cu^{2+} ions withdraw electrons from the Si conduction band (or inject holes into the Si valence band) and are electrolessly deposited on the Si surface as Cu nanoparticles. The Cu nanoparticles act as the microscopic cathode and catalyze the reduction of the oxidizing agent HNO_3. Simultaneously, due to hole injection, the Si surface underneath the Cu nanoparticles is oxidized and then dissolved by HF. As a result, the Si surface surrounding the Cu nanoparticles is etched and the Cu nanoparticles sink into the wafer.

In the Cu-ACE, generally, a separate oxidant is used, like HNO_3 in our case, since according to widely accepted theory, the Cu acts only as a catalyst [53], and thus an additional chemical is needed to increase hole generation for oxidation of the Si.

The electroless deposition of the Cu nanoparticles is preferred to start at the defective sites due to the weaker Si-Si bond in the defect region, which made it simpler for the oxidant in the solution to capture electrons [54]. This explains the selective etching property of Cu-ACE in the laser-modified regions. Unlike Cu, for other catalysts such as Ag, Au, and Pt, the initial deposition occurs on both ideal and defective sites [55]. However, prolonged etching time can cause defect-free regions also to be etched for the Cu-ACE. To effectively remove the laser-modified regions, a polished Si wafer is used in our study since it has less defects on the surface, so initial preferential deposition starts mostly at the laser-defective regions.

CHAPTER 3

3D MICROPILLAR ARRAYS FABRICATION ON SILICON WAFER

In this chapter, it is aimed to fabricate high quality, regular 3D micropillar arrays on c-Si wafer using ns-pulsed infrared laser for potential application in radial junction solar cell. Since light absorption performance of the micropillar arrays strongly depends on the geometry of the pillars, a systematic study was carried out to determine optimum pillar dimensions with optimum etching duration.

3.1 Introduction

Light absorption and charge collection are two fundamental requirements for efficient energy conversion in a photovoltaic device. The light absorption generates electron and hole pairs which are then separated by a built-in electric field of the depletion region at pn junction. The separated minority charge carriers (electrons and holes) are collected by the metal contacts, creating an electric current flowing through the external circuit.

Since silicon is an indirect bandgap material, the light absorption at long wavelengths is poor. Thus, in planar junction c-Si solar cells, wafer thickness should be greater than optical thickness for efficient light absorption. In fact, in order to absorb 90% of the incident light above the bandgap, a c-Si wafer thicker than 125 μm is required [56]. In the planar junction solar cell (Figure 3.1.a), the light absorption direction is the same as the carrier collection direction. Also, the width of the depletion region is much smaller than the light absorption length so that most of the photogenerated carriers occur outside of the depletion region. As a result of these, the minority carrier diffusion length should not be shorter than the wafer thickness to be able to effectively collect photogenerated carriers with the front and bottom electrode of the

solar cell. Achieving such long minority carrier diffusion lengths requires extremely high pure, high cost single c-Si material.

Recently, c-Si micropillar arrays based solar cells have been proposed as a promising device design for next generation solar cells [57-59]. This design (Figure 3.1.b) consists of arrays of silicon micrometer-sized pillars each with 3D radial pn junctions instead of a 2D planar pn junction in the conventional solar cell. Compared to the planar surface, the structured surface with micropillar arrays has a higher surface area and efficient light trapping where multiple interactions (reflections and refractions) of the light within the gaps between the pillars increase light absorption probability due to increased optical path length. Therefore, with proper design and photon management, the pillar arrays can extend the light absorption over a broad range of wavelength even beyond the classical absorption limit [60]. In addition, 3D radial pn junction geometry exhibits efficient carrier collection since minority carrier collection occurs in the relatively short radial direction which is orthogonal to the direction of light absorption [61]. Therefore, instead of using high purity, high cost single c-Si material, equally efficient solar cells can be developed from low purity, low cost c-Si material that has short minority carrier diffusion length.

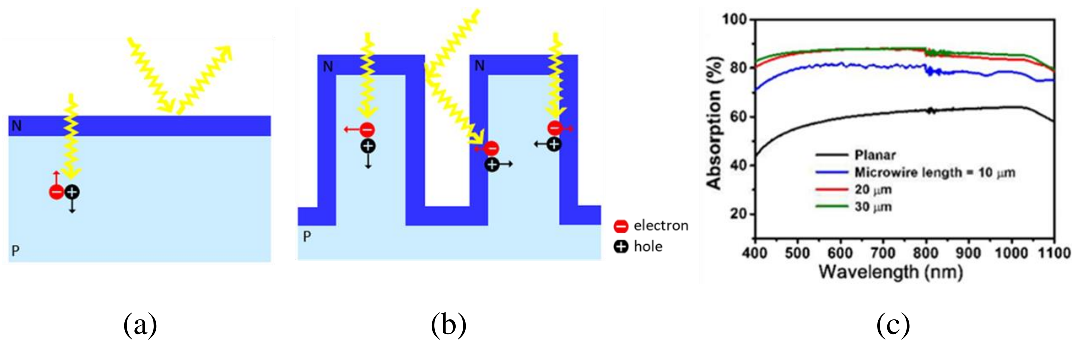

(a) (b) (c)

Figure 3.1 Schematic representation of light absorption and photo-generated carrier separation in a planar (a) and radial (b) junction solar cell. (c) Absorption spectra of planar Si and microwire arrays with different lengths. (Each microwire has a diameter of 2 μm and spacing between the wires is 2μm.)

It is expected that the light absorption of the pillars improves with increased wire length because longer wires increase the optical path length by allowing more light to be scattered between the wires, and hence more light is absorbed into the pillars.

However, as the pillar length increases, the light absorption reaches saturation. As seen in Figure 3.1.c, light absorption increases up to a wire length of approximately 20 μm but then becomes saturated [62]. The reason for this limitation in light absorption is top surface reflection, which is independent of the micropillar length.

Si nanopillar arrays are black in color and exhibit superior light absorption properties. However, the reported efficiencies c-Si nanopillar solar cells are much lower than the conventional c-Si solar cells because the nanopillar arrays have a very high surface-to-volume ratio resulting in significant surface recombination. Furthermore, the pn junction in Si nanopillars can be fully doped since the radius of the nanopillar is smaller than the junction depth of conventional thermal doping, i.e. ~500 nm. This fully depleted pn junction can cause serious Auger recombination, reducing the efficiency of the cell [59, 62]. In contrast, the micropillar arrays with a radius greater than 1 μm not only enhance light absorption but also allow the formation of a stable radial junction by using conventional doping procedures [63].

As shown in theoretical studies [61, 64, 65], the performance of radial junction pillar array cells strongly depends on the dimensions of the pillars including diameter, length, and period. However, not enough experimental studies have been conducted to verify these predictions.

Based on these considerations for the micropillar geometry, we are going to produce high-quality, 3D micropillar arrays on c-Si by using our novel ns-laser 3D structuring technique coupled with Cu-ACE.

3.2 Experimental

3.2.1 Laser Setup

We used a custom-built fiber laser system that operates at a central wavelength of 1550 nm, producing pulse duration around 6 ns with average power up to 5 W. The power amplifier is based on Er-Yb co-doped fiber, and the repetition rate can be

adjusted in the range of 100 kHz to 1 MHz. The schematic of the laser setup is shown in Figure 3.2.

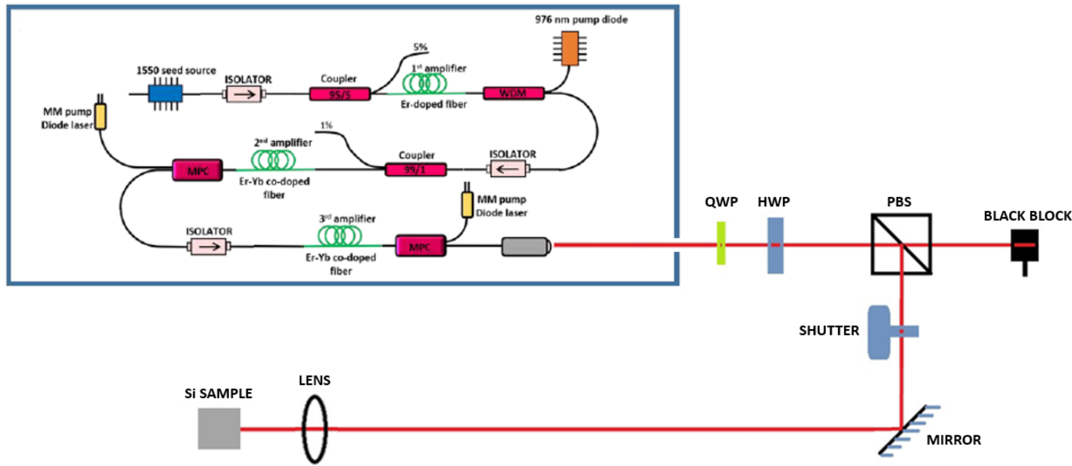

Figure 3.2 Schematic of custom-built 1550 nm, ns-pulsed laser setup. MM, multimode; MPC, multiple-port pump-signal combiner; WDM, wavelength division multiplexer; QWP, quarter-wave plate; HWP, half-wave plate; PBS, polarizing beam splitter.

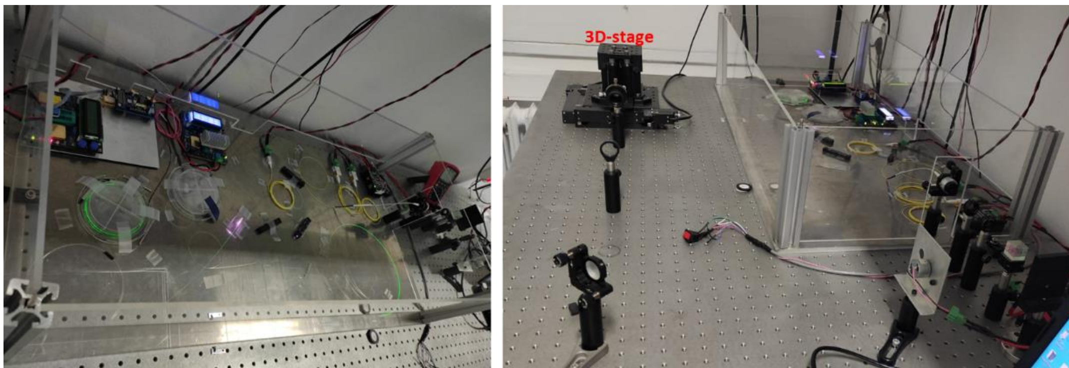

Figure 3.3 Photographs of ns-laser setup.

At the end of the laser system, a high-resolution computer-controlled 3-axis motorized translation stage is utilized for laser alignment and controllable sample processing. To tightly focus the output laser beam inside silicon, an aspheric lens is used with f=8 mm. The power and polarization of the laser beam are controlled by HWP and QWP. The laser beam is divided into horizontal and vertical directions using the polarizing beam splitter. All laser processing experiments were carried out at room temperature and in ambient atmosphere.

3.2.2 Laser Surface Processing

The Si samples are held to the translation stage with neodymium magnets. To focus the laser beam precisely on the Si surface, we move the stage back and forth until the intensity of the beam is minimal on the IR detector card held behind the sample. This maximizes the laser intensity on the Si surface and creates a white spark due to plasma as shown in Figure 3.4.

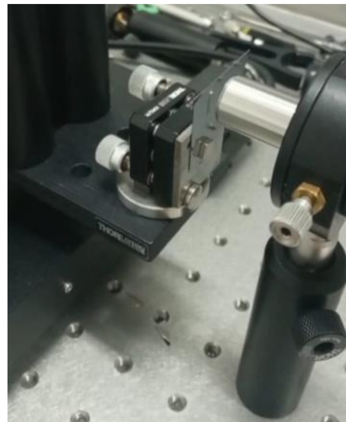

Figure 3.4 Plasma generation on Si surface during laser processing.

The Si samples were raster scanned on a plane perpendicular to the laser propagation direction with a 5 mm/s scan speed as illustrated in Figure 3.5. The raster scan generates pillar structures on the sample. The focused laser on the scanned region induces modifications in the focal volume due to multiphoton absorption.

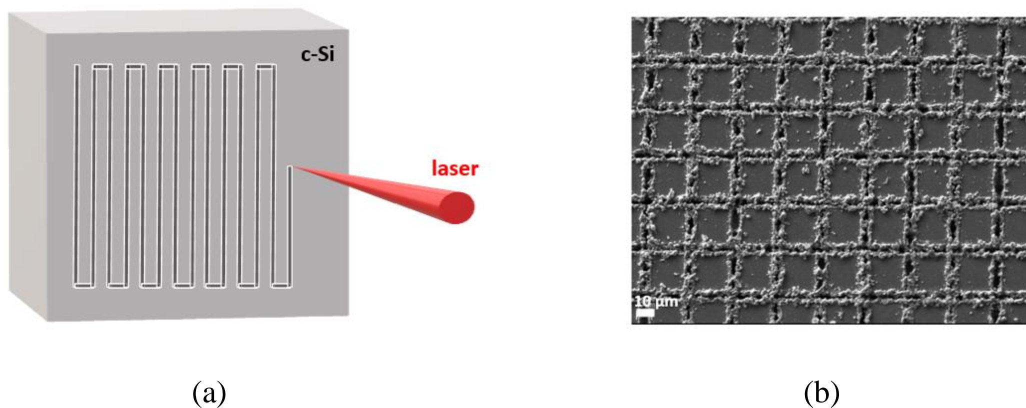

(a) (b)

Figure 3.5 (a) Schematic representation of raster scan on Si surface. (b) SEM image of pillar structures formed on c-Si wafer after raster scan.

In the surface processing, the laser was operated with a pulse duration of 6 ns. And, a repetition rate of 100 kHz that corresponds to a pulse energy of 6.5 μJ was utilized. Although modification treshold was lower than 6.5 μJ, the lower pulse energies failed to produce a fully structured area.

At the given pulse energy, the peak power is calculated as ~1083 W, but about 30% of the incident beam is reflected for the 1550 nm wavelength, thus the peak power of the pulse in the Si is ~758 W. To estimate the intensity at the focal point, the laser spot size (s) in the silicon needs to be determined. For this, first, the numerical aperture (NA) in air was calculated as ~0.47 from NA=sin(D/2f), where D is the diameter of the light illuminating the lens and measured as ~7.8 mm. Accordingly, from Snell's law, the NA_{Si} in the silicon was found to be ~0.14. Then, using the formula $s=2\lambda/\pi \ NA_{Si}$ for the Gaussian laser beam, the laser spot size in the silicon were calculated as ~7.3 μm. Lastly, from the intensity definiton for the pulsed laser, I=peak power/beam area, the intensity at the focal spot was estimated to be ~1.8 GW/cm^2. This value is also close to the threshold intensity required for subsurface modifications indicated in section 2.1.1.

3.2.3 Micropillar Fabrication Procedure

The micropillar fabrication procedure started with laser structuring. Single side polished, 280 μm thick, single-crystalline p-type Si wafer with <100> orientation and 1-10 Ω.cm resistivity were used in the fabrication. As seen in Figure 3.6, we prepared seven identical sample sets, each containing 2 mm × 2 mm structured regions with laser step sizes of 20 μm, 30 μm, 40 μm, 50 μm, and 60 μm. The laser step size indicates the period of the pillar structures, i.e. the center-to-center distance of the pillars. Then, selective etching of the laser-modified regions was performed using the Cu-ACE recipe specified in the previous chapter. Each set was immersed in ~35 ml of Cu-ACE solution and etched for different times ranging from 10 to 60 minutes. Before and after etching, the samples were cleaned in diluted HF for about 30 seconds and rinsed with DI water. Only, the first set was left unetched for

reference. The process was carried out at room temperature and it was observed that solution temperature decreased over time. Different etching times were employed to create pillars with various depths, and different laser step sizes were utilized to have varied micropillars widths.

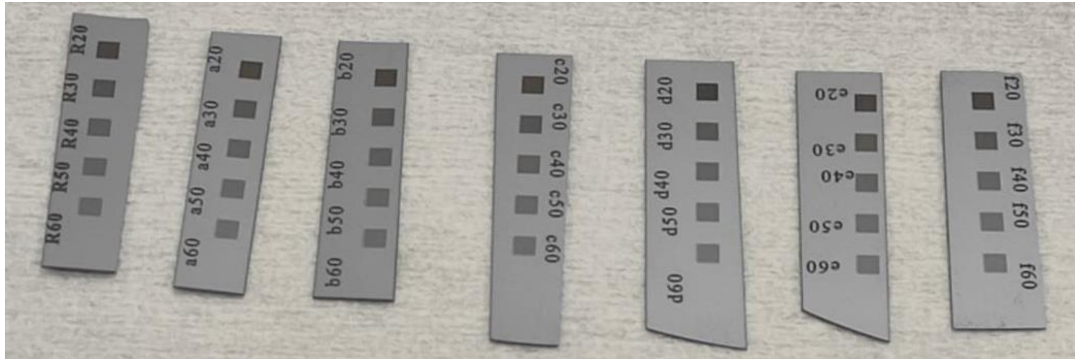

Figure 3.6 ns-laser structured c-Si sample sets each with 20 µm, 30 µm, 40 µm, 50 µm, and 60 µm laser step sizes.

Scanning Electron Microscopy (SEM) imaging was performed for the analysis of the micropillar structures. Figure 3.7 shows the SEM images of 10 minutes etched sample set that shows periodic Si micropillar arrays for each structured region. For all laser step sizes, smooth micropillar surfaces appear to form with negligible defects. For 20 minutes etched sample, again the pillar structures are in good quality as seen in Figure 3.8, but 20 minutes etching is a bit excessive for the 20 µm step size. For the 30 minutes etched sample, the micropillars with the 30 µm step size are over-etched, but interestingly this is not the case for the 20 µm step size. These two structured regions belong to the same set, and hence were etched in the same beaker. Therefore, the difference is not related to the etching solution, but may be caused by a power fluctuation or a shift of focus due to a mechanical effect during laser structuring. At higher etching times, the larger step-sized structures maintain their pillar form and show acceptable quality, whereas smaller step-sized pillars begin to deteriorate or even are etched completely for the 20 µm step size.

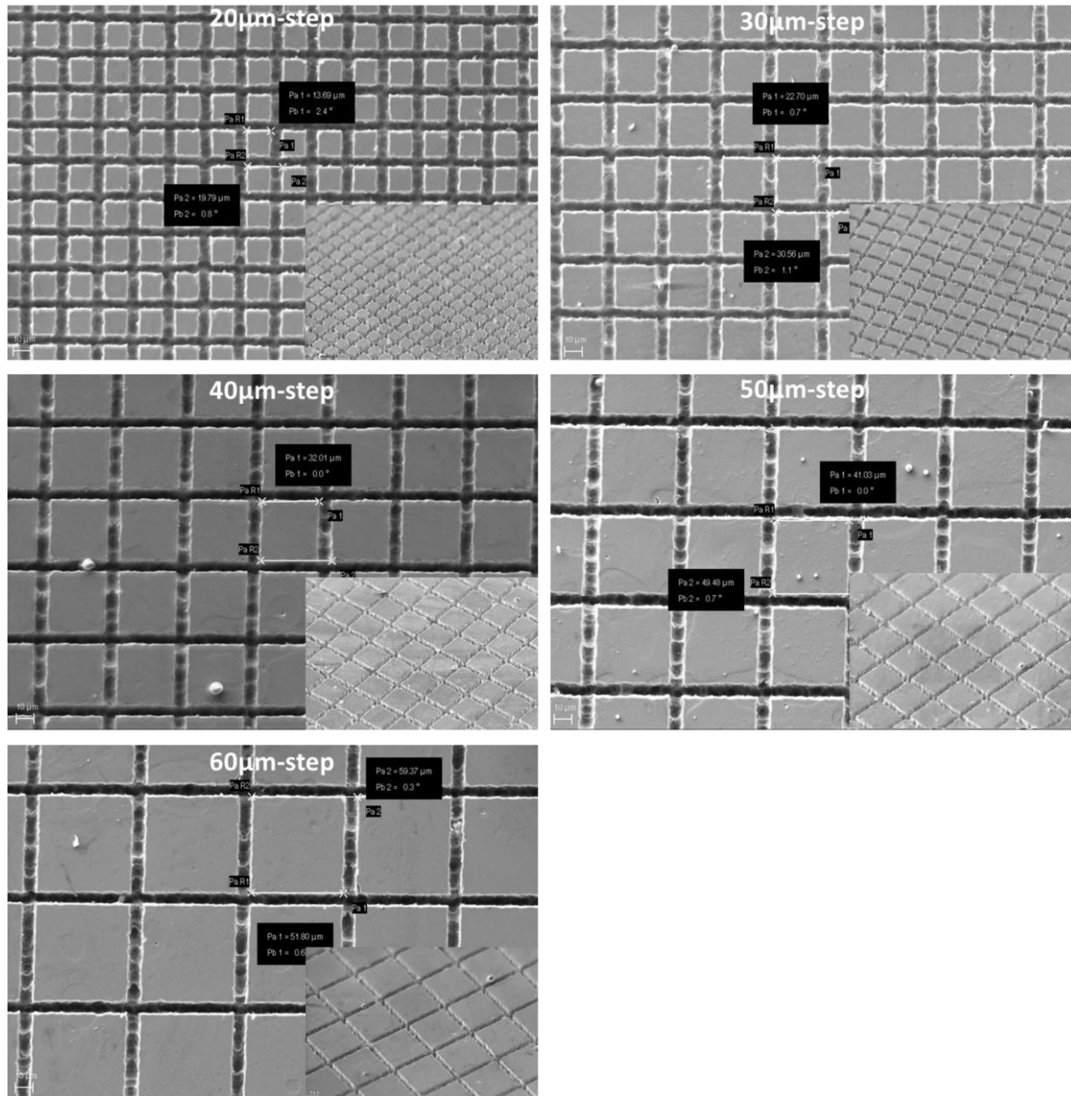

Figure 3.7 SEM images of 10 min. etched sample set showing Si micropillar arrays at 1000X magnification.

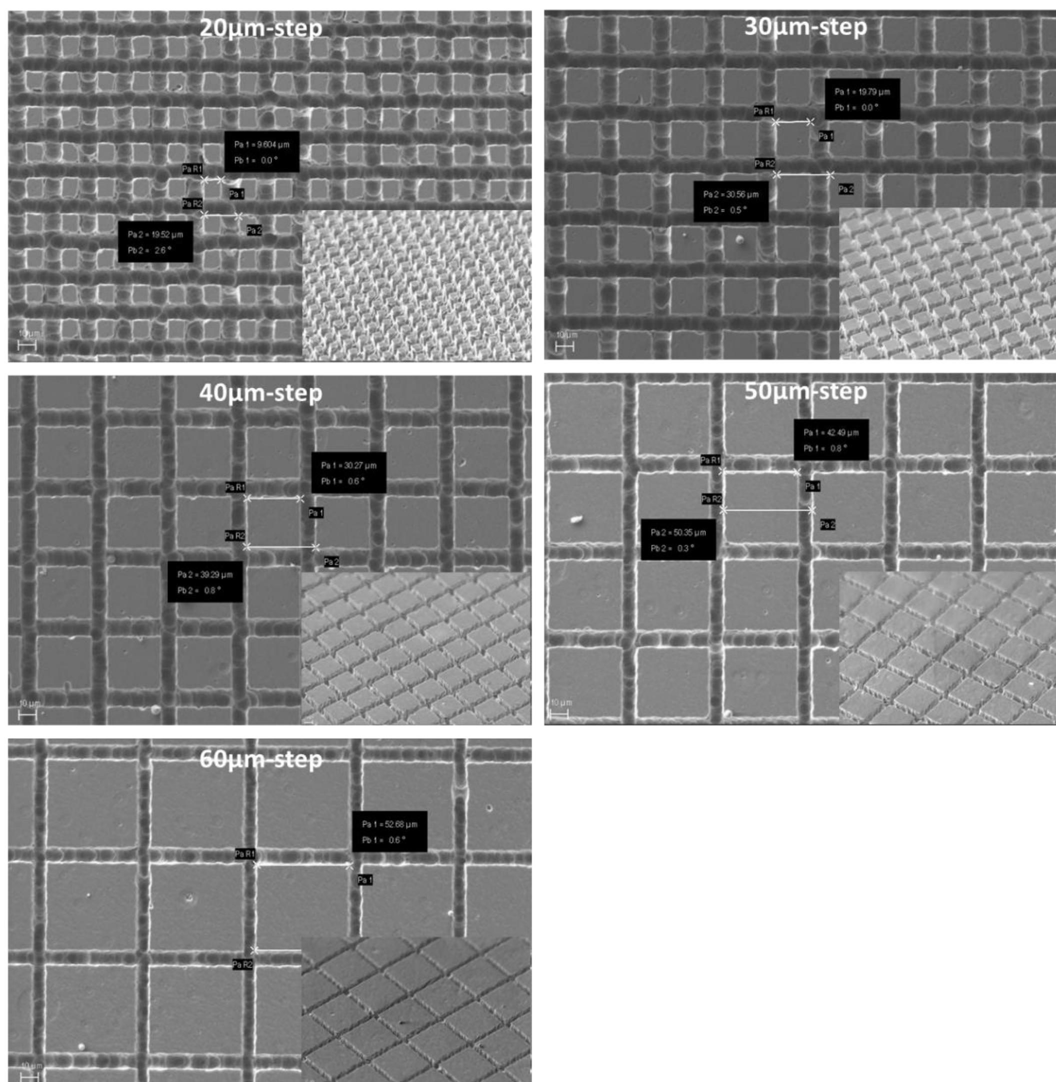

Figure 3.8 SEM images of 20 min. etched sample set showing Si micropillar arrays at 1000X magnification.

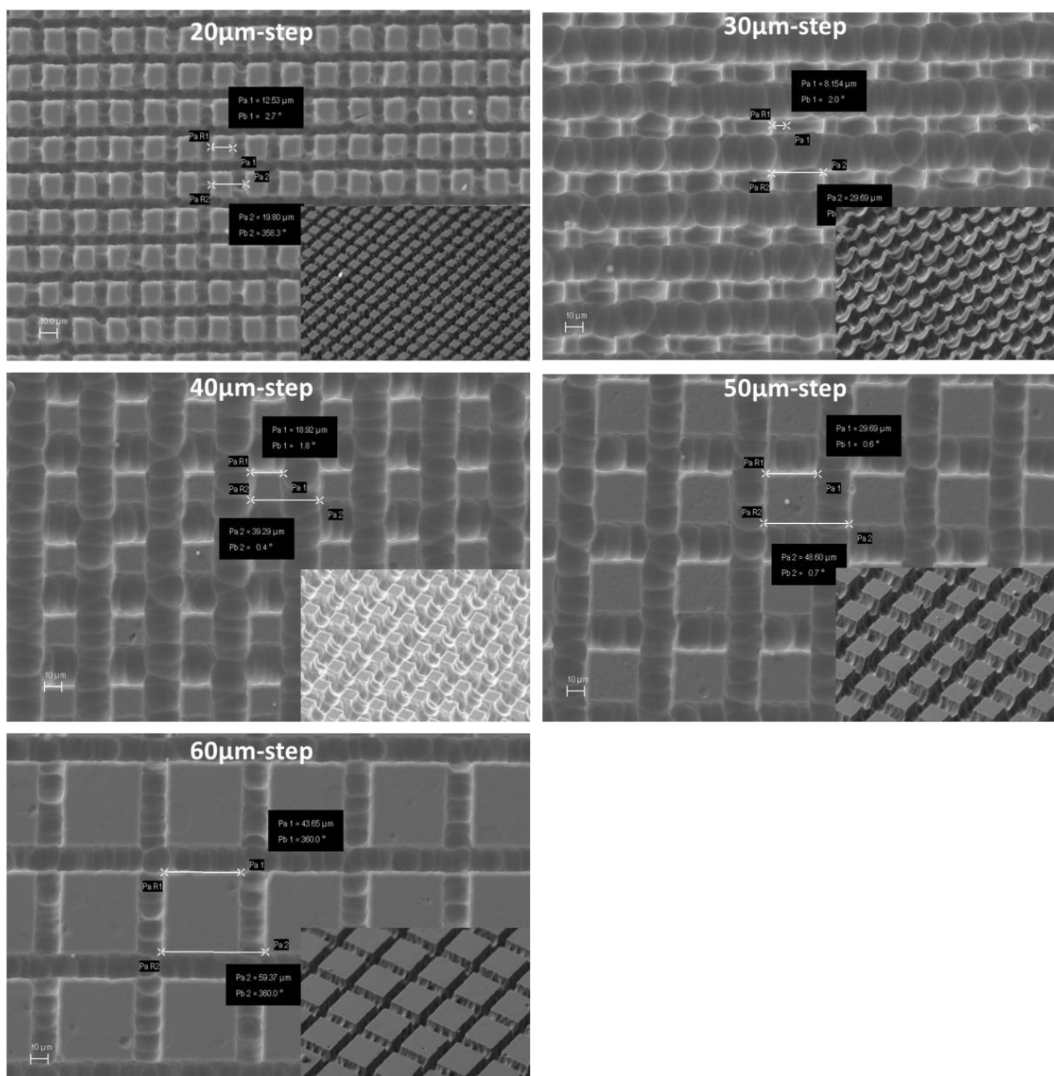

Figure 3.9 SEM images of 30 min. etched sample set showing Si micropillar arrays at 1000X magnification.

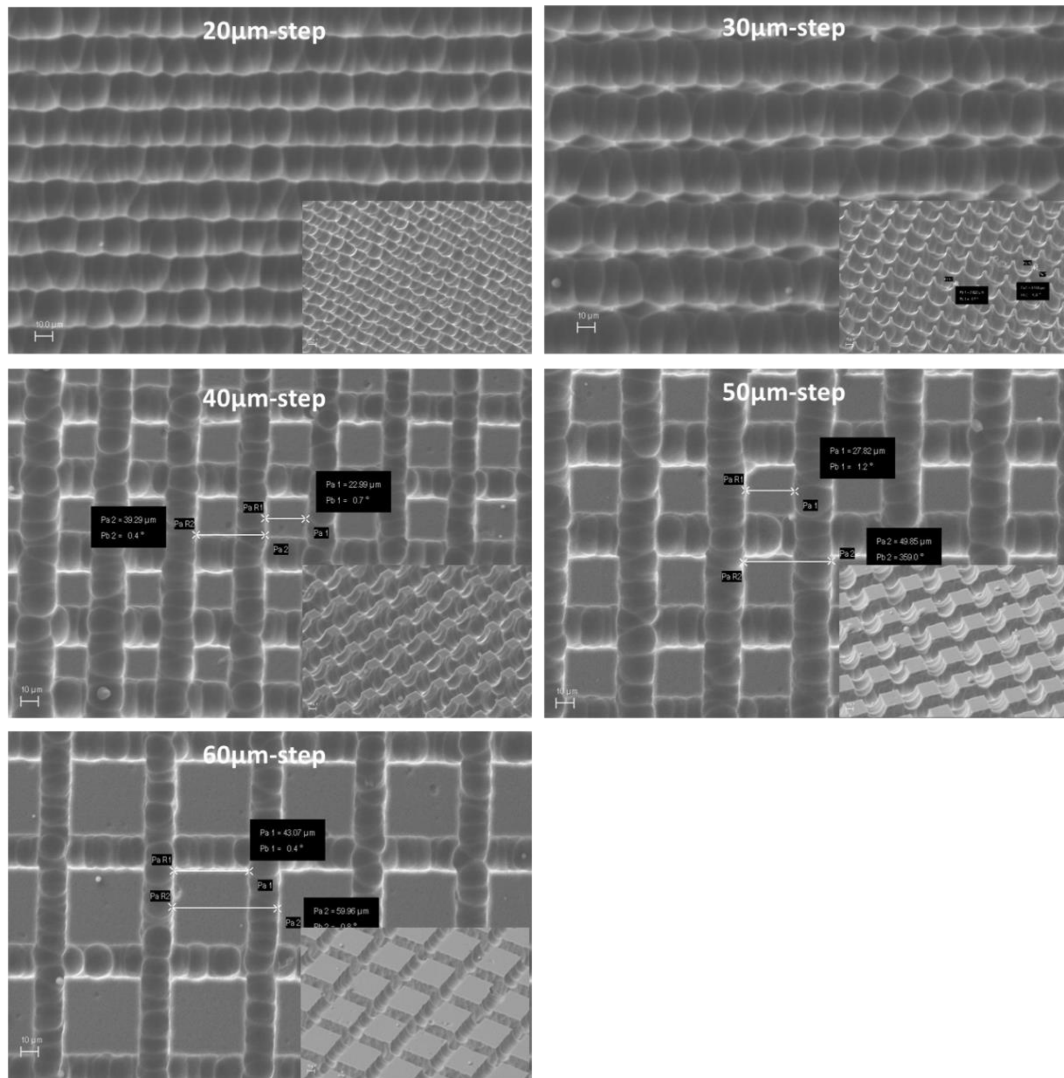

Figure 3.10 SEM images of 40 min. etched sample set showing Si micropillar arrays at 1000X magnification.

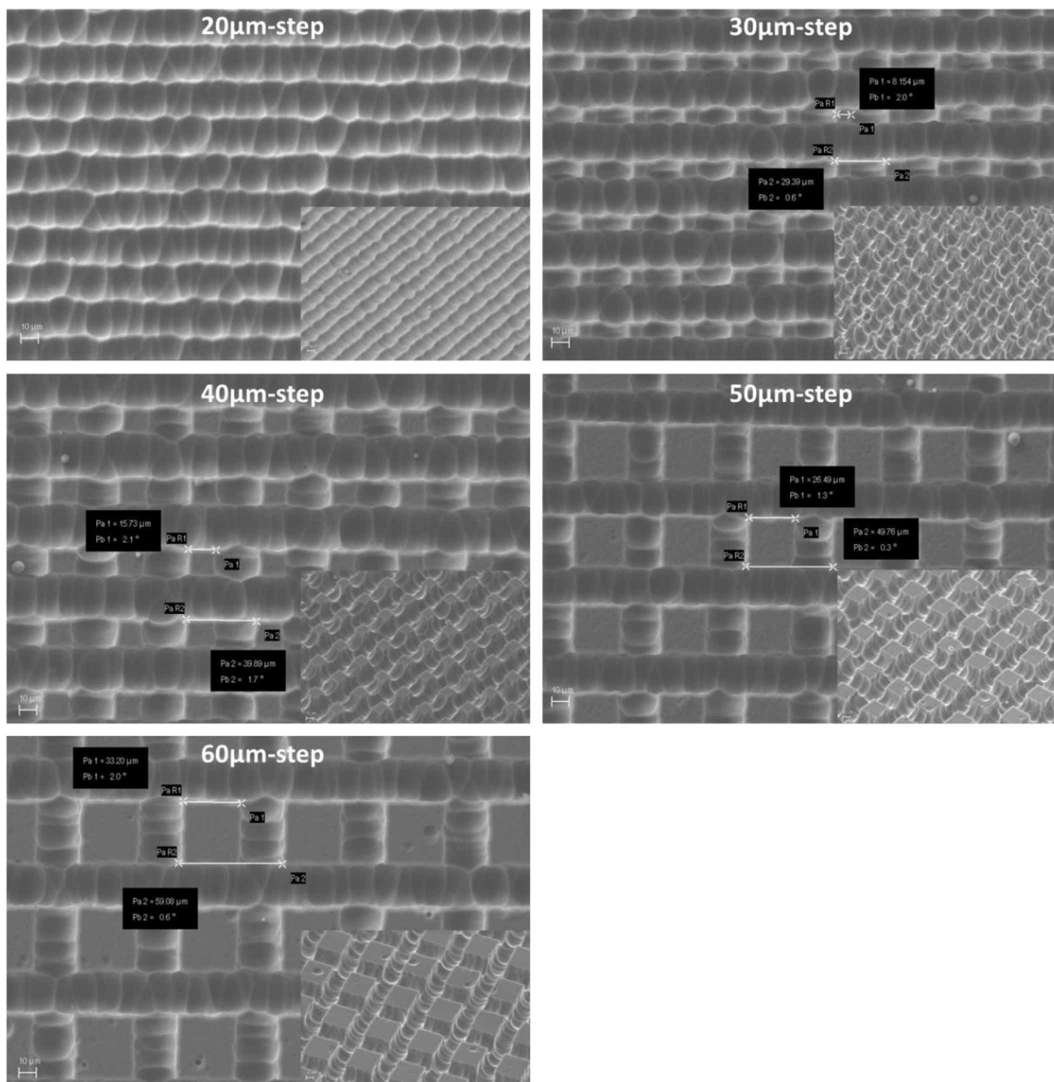

Figure 3.11 SEM images of 50 min. etched sample set showing Si micropillar arrays at 1000X magnification.

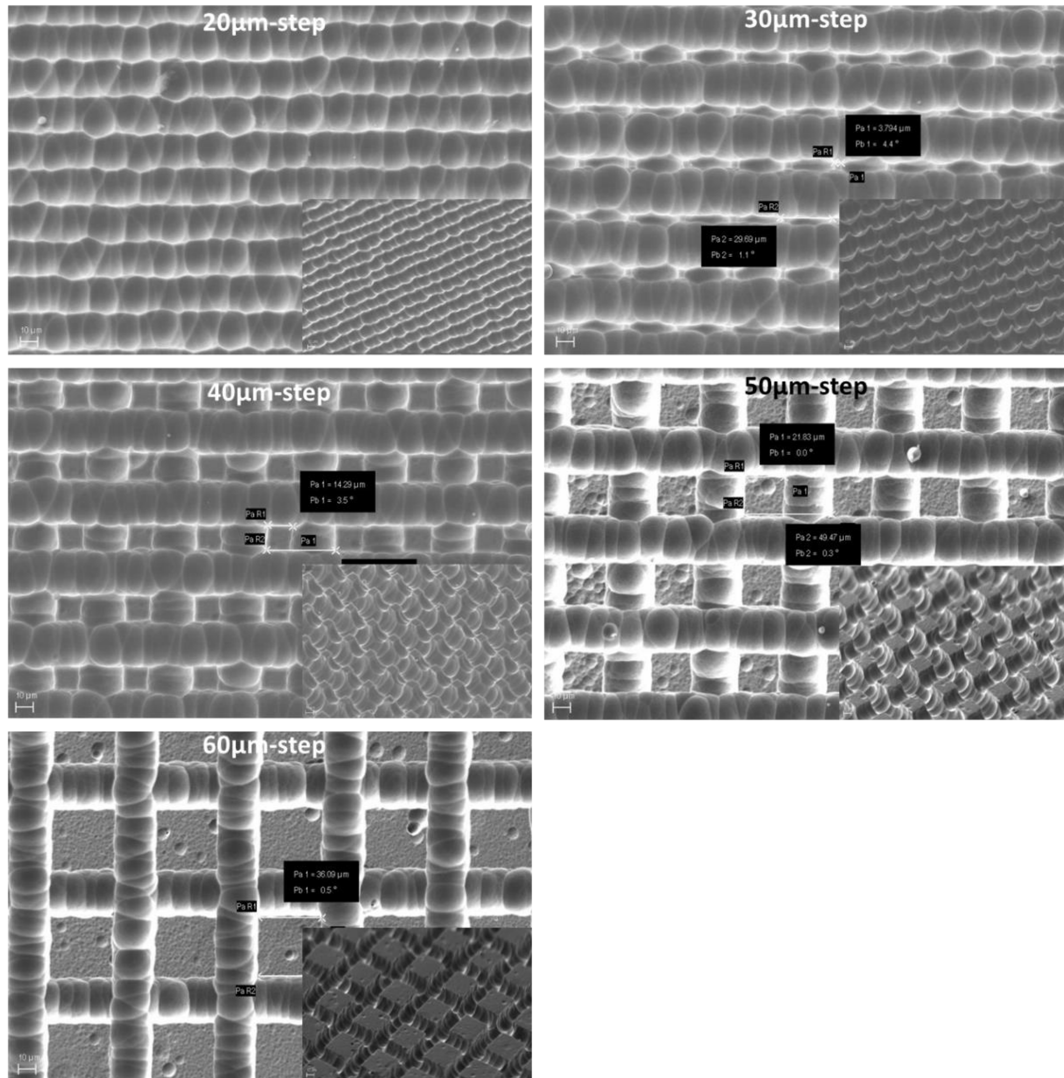

Figure 3.12 SEM images of 60 min. etched sample set showing Si micropillar arrays at 1000X magnification.

The longest pillar structures were formed at 60 minutes of etching time for 50 µm. and 60 µm step sizes. Figure 3.13 shows the longest pillar structures which are around 26 µm. On the other hand, the 60 minutes of etching creates micron-sized voids on the surface of the pillars, disrupting the smoothness of the surface.

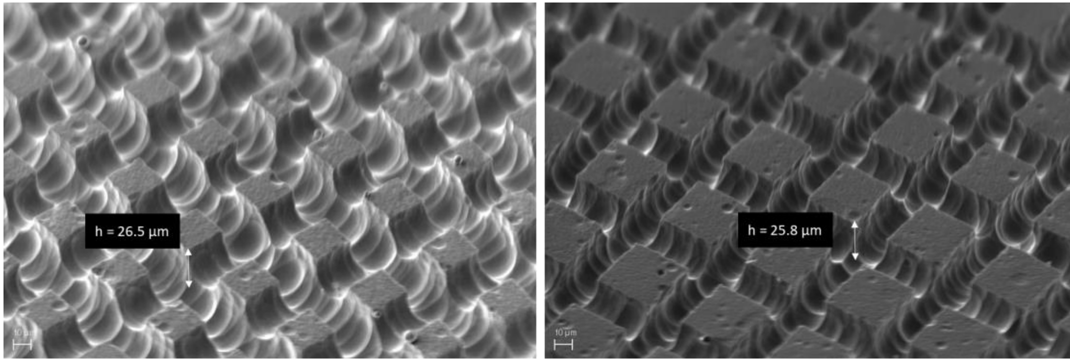

(a) (b)

Figure 3.13 45^0 tilted SEM images of 60 min. etched sample showing Si micropillar depths at 1000X magnification for (a) 50 µm and (b) 60 µm step sizes.

As expected, measured micropillar widths generally tend to decrease with increasing etching time, as seen in Figure 14. And, 1 or 2- micron deviations from the decreasing trend of pillar widths can be attributed to measurement errors. The highest etching rates are observed between 10 and 20 minutes. In this study, it is important to find optimal etching time since high etching time increases the gap between the pillars, which can reduce the absorption performance of the pillars because of less multiple scattering of light.

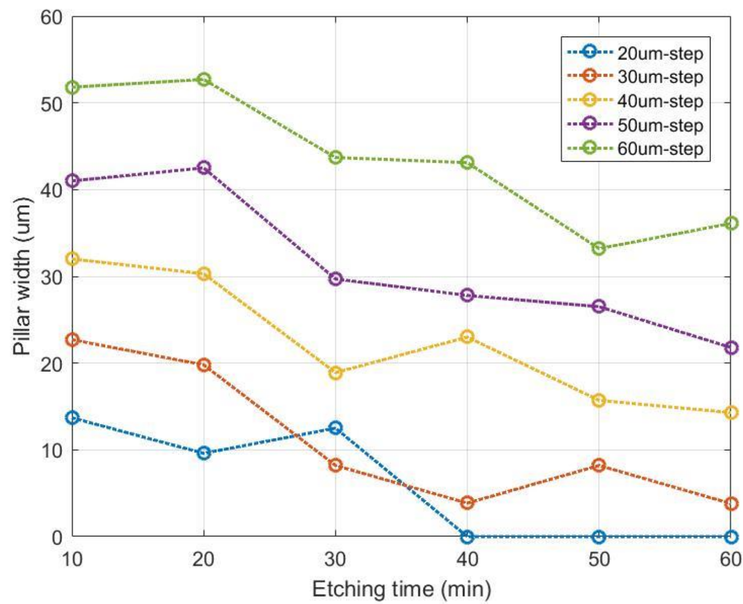

Figure 3.14 Micropillar width variation with increasing etching time.

In Figure 3.15, reflection spectrums of the same laser step size are shown in one graph according to the etching times. The wavelength spectrum between 350 nm and 1100 nm was utilized due to weak photon absorption for c-Si above 1100 nm and very low power density below 350 nm. In the graphs, the reflection spectra of the

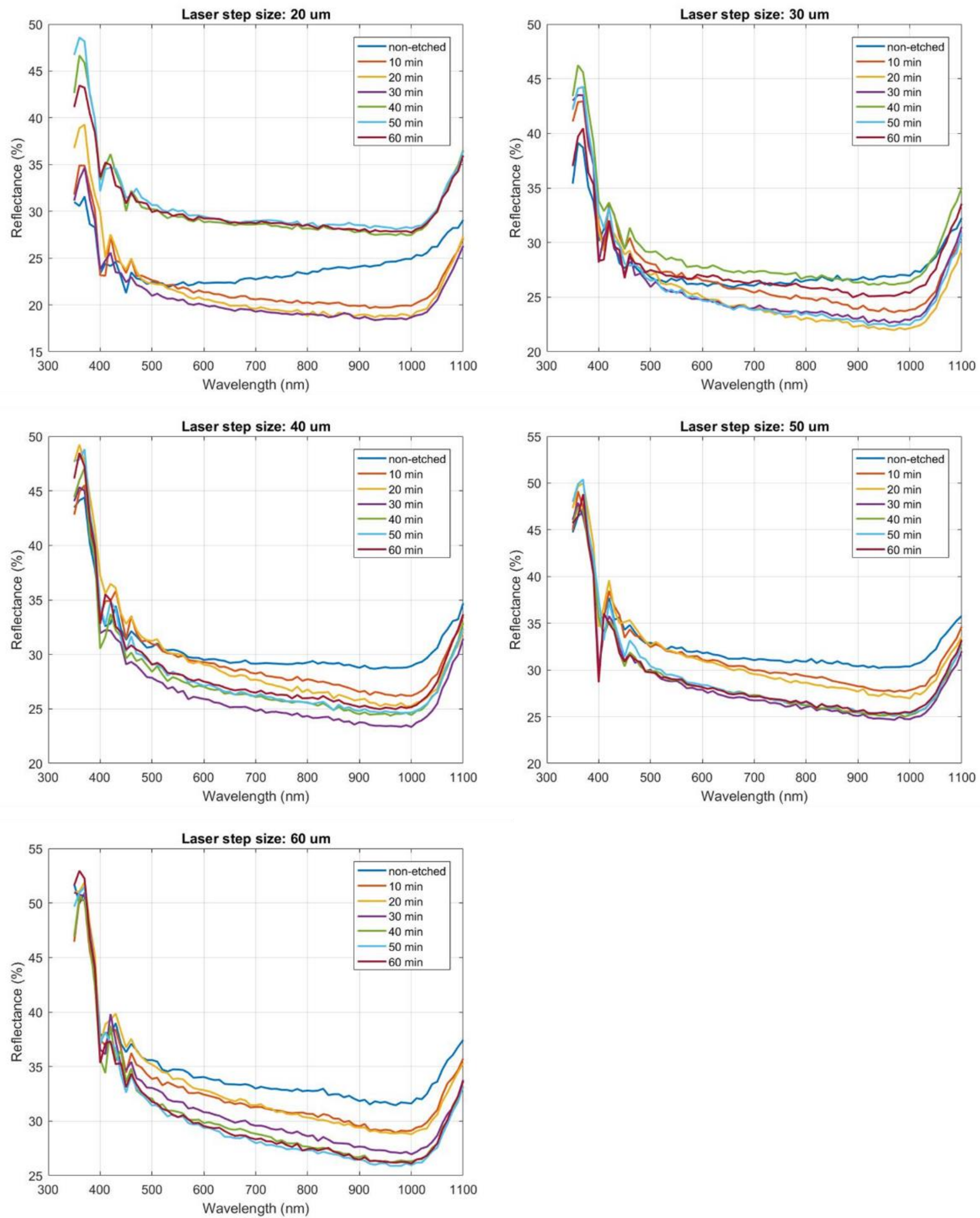

Figure 3.15 Reflectance spectrums of micropillar structures. (Each graph shows the reflectance spectra for the same laser step size etched between 10 and 60 min.).

non-etched sample are also included for comparison. It is clearly seen that at the 20 µm step size, non-etched structures show better absorption performance than etched structures between 30-60 minutes.

In order to quantitively compare reflection curves, the weighted reflection values based on AM1.5G were calculated using Equation 3.1,

$$WR = \frac{\int R(\lambda)S(\lambda)d\lambda}{\int S(\lambda)d\lambda} \tag{3.1}$$

where, S(λ)is the intensity of solar radiation and R(λ) is the surface reflectance at a given wavelength λ [66].

From the weighted reflection results given in Figure 3.16, it can be seen that the lower step-sized pillars exhibit better absorbance, since narrower pillars have higher surface increase factor at the same etching duration. However, for the 20 µm and 30 µm step sizes, the reflection starts to increase after 30 minutes of etching because of deteroited pillar structures. Indeed, after certain time excessive etching cause for all different step size to reduce absorption property. In fact, after a certain time, excessive etching reduces the absorption property for all different step-sized pillars.

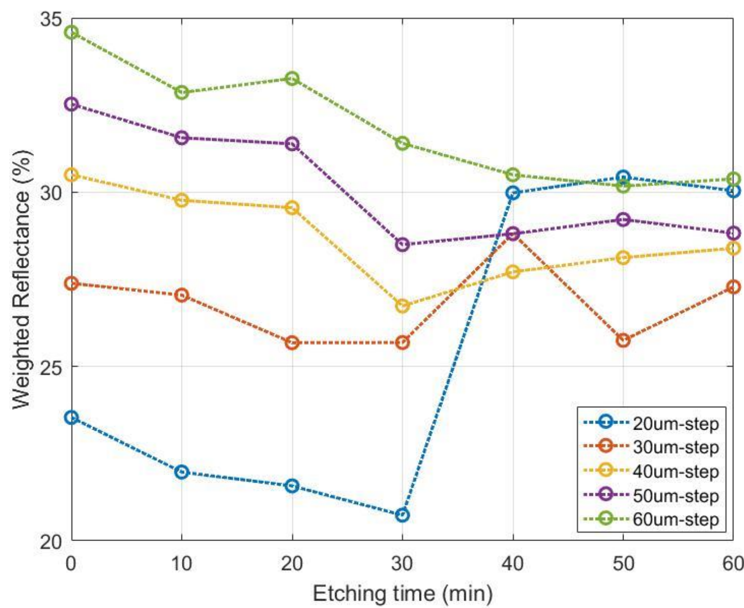

Figure 3.16 Weighted reflectance for different step-sized pillars etched between 10 and 60 min.

After detailed analysis of the SEM and reflectance measurements, it appears that 20 μm step-sized pillars etched for 10 minutes yields the best result. Although the weighted reflectance values of 20 μm step-sized pillars etched for 10 and 20 minutes are almost the same, better quality micropillar structures were generated with 10 minutes etching duration. Figure 3.17 shows the tilted SEM image of high quality 3D micropillar arrays on c-Si wafer produced from 20 μm step-sized pillars etched for 10 minutes.

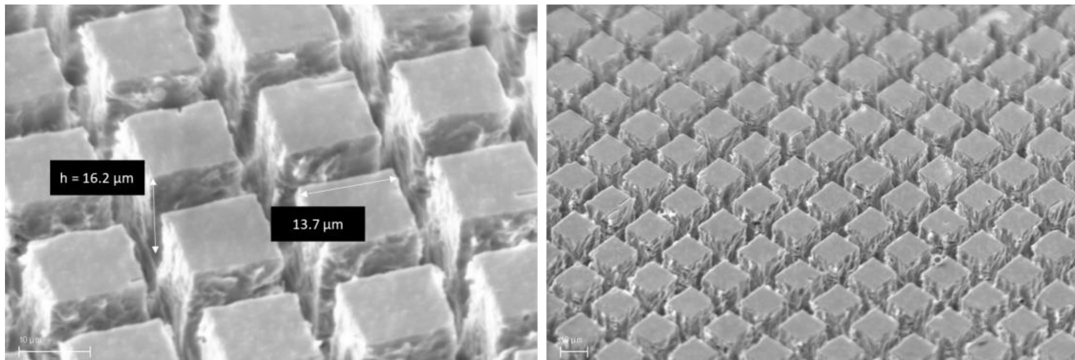

Figure 3.17 45^0 tilted SEM images of 10 min. etched sample showing 3D periodic Si micropillar structures with 20 μm step size. (Process area: 2 mm × 2 mm).

For further analysis, we prepared 5 mm × 5 mm structured regions with 20 μm step size on Si wafers and etched them for 10 and 15 minutes. The SEM images of the 10 and 15 minutes etched samples are seen in Figures 3.18 and 3.19, respectively. After 10 minutes of etching, the pillars with 13.7 μm width and 17.9 μm length were fabricated, which are similar to previous results. Etching for 15 minutes, increased the pilllar length to 19.7 μm and decreased the pillar width to 12.5 μm. Figure 3.19 shows the reflection spectrum and Table 3.1 indicates corresponding weighted reflection values for 10 and 15 minutes etched samples. For comparision, the reclectance spectra of unstructured Si and non-etched structured Si were also measured. The weighted reflection value was obtained around % 17.5 for 10 and 15 minutes etching. This can be explained by nearly same surface increase factor calculated for their unit pillar.

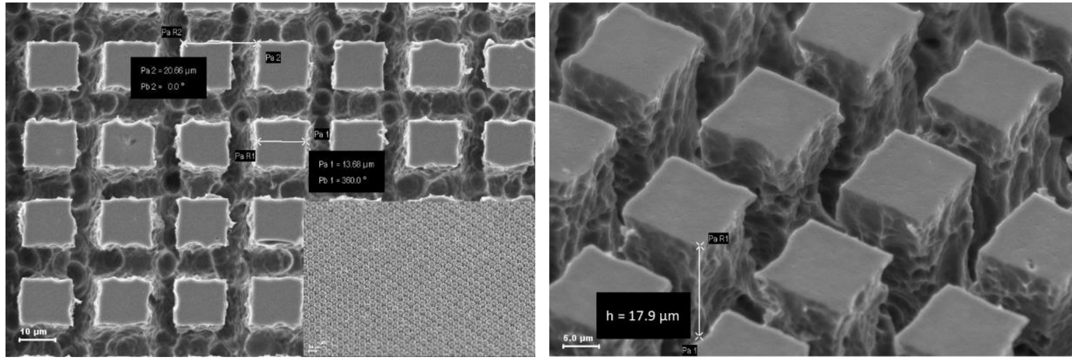

Figure 3.18 SEM images of 10 min. etched sample with 20 µm step size. (Process area: 5 mm × 5 mm).

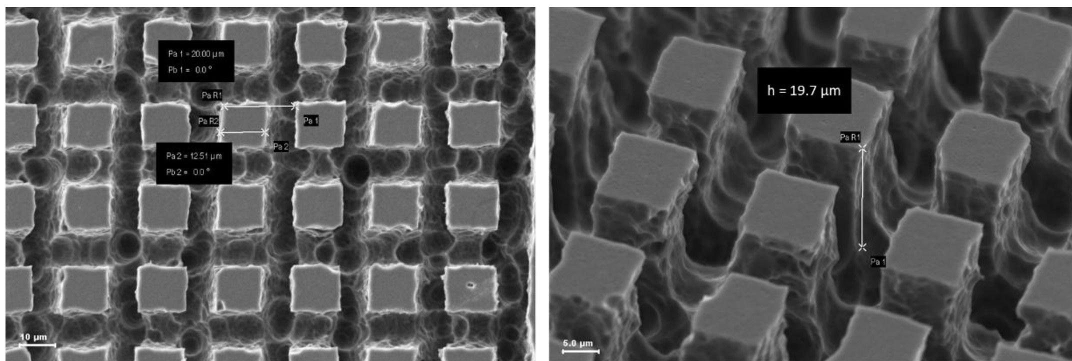

Figure 3.19 SEM images of 15 min. etched sample with 20 µm step size. (Process area: 5 mm × 5 mm).

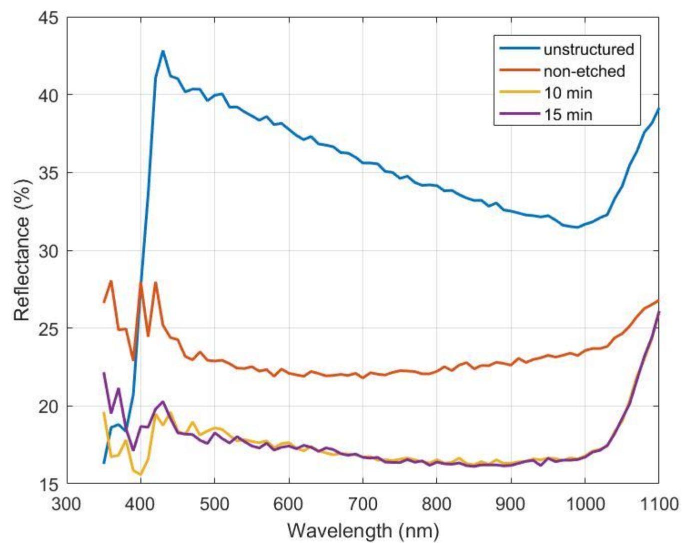

Figure 3.20 Reflection spectra of non-etched, 10 min. etched, and 15 min. etched samples with 20 µm step-sized pillars. (Process area: 5 mm × 5 mm).

Table 3.1 Weighted reflection of non-etched, 10 min. etched, and 15 min. etched samples with 20 µm step-sized pillars. (Process area: 5 mm × 5 mm).

Weighted Reflection (%)			
unstructured	non-etched	10 min. etched	15 min. etched
35.70	23.03	17.46	17.52

In summary, the highest quality 3D micropillar structures with dimensions of 13.5±1 µm in width and 17±1 µm in length were produced using 20 µm laser step-sized pillars etched for 10 minutes. The dimensions of the created pillar structures are also suitable for radial pn junction formation. The longer pillars were not prefered since using pillars longer than 20 µm does not contribute significantly to the absorption. Additionaly, shorter micropillars allow better radial junction formation on the pillar surface by using conventional doping methods.

3.2.3.1 Sample Cleaning

In order to remove metallic (i.e. Cu) and organic contaminations, after micropillar fabrication, Si samples were cleaned by RCA 1 and RCA 2 standard cleaning procedures. The RCA 1 containing $NH_4OH:H_2O_2:H_2O$ with a volume ratio of 1:1:5 at 70±5°C was applied for 15 minutes to clean organic contaminations. And, RCA 2 containing $HCl:H_2O_2:H_2O$ with a volume ratio of 1:1:5 at 70±5°C was applied for 15 minutes to remove metallic contaminations.

Residual Cu nanoparticles can have fatal effects on device performance and must be removed effectively. Thus, as final cleaning, $HNO_3:H_2O$ with a volumetric ratio of 2.5:1 at room temperature was utilized to completely remove the Cu residuals from the micropillar surface. To ensure no copper remained on the sample surface, SIMS analysis was performed.

3.2.4 SIMS Analysis

Secondary ion mass spectrometry (SIMS) is a very sensitive technique for analyzing the surface material composition to a depth of 1 to 2 nm by sputtering the sample surface with a focused primary ion beam and collecting secondary ions ejected from the sample surface.

The SIMS depth profile of the cleaned sample is presented in Figure 3.21. As seen in the figure, the distribution of Cu is almost zero. However, the distributions of other metallic pollutants such as Ca, Na, K, Fe, and Mg are significant. Therefore, we could not form radial junctions on the Si micropillars to not contaminate the diffusion furnace. To prevent contamination of the sample, the micropillar fabrication needs to be conducted in a highly controlled clean room environment with specialized equipment (i.e. quartz beaker, sample holder, etc.).

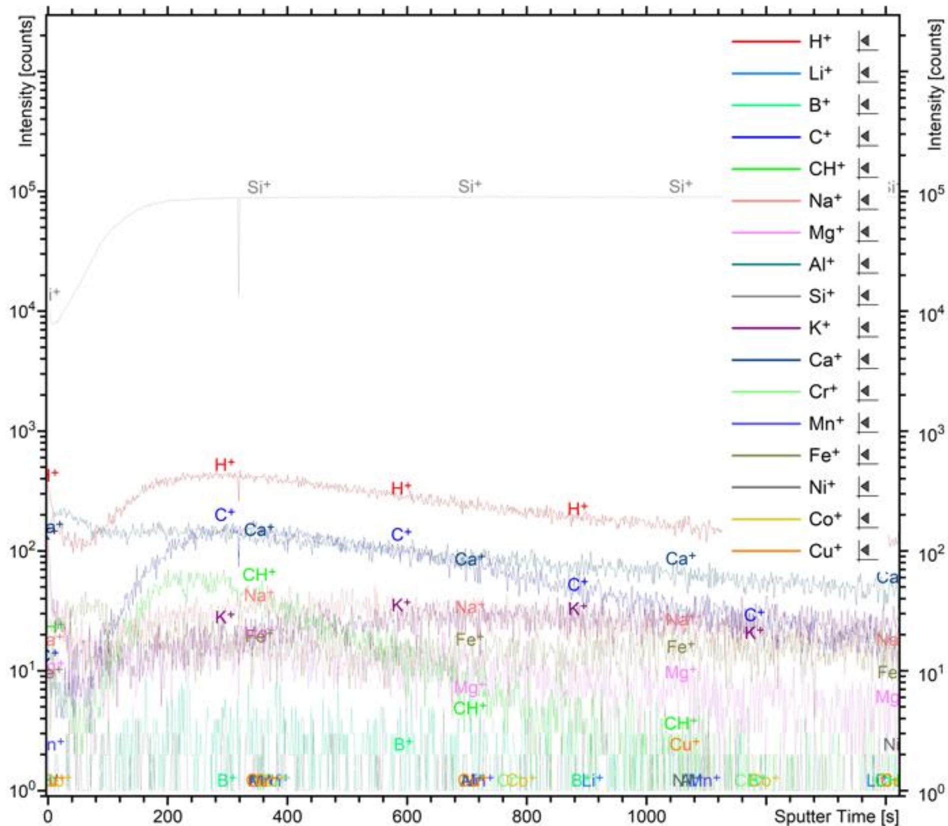

Figure 3.21 SIMS profile on micropillar surface

CHAPTER 4

FABRICATION OF NEUTRAL-COLORED TRANSPARENT SILICON WAFER VIA 3D MICROHOLE ARRAYS

In this chapter, neutral-colored transparent c-Si substrate was fabricated for potential use in transparent solar cells. Specially designed 3D microhole arrays, indistinguishable to human eye, were produced through 280 μm thick c-Si wafer with our novel maskless laser-induced method.

4.1 Introduction

Transparent photovoltaics (TPVs) is a highly desirable technology for applications where the use of traditional opaque solar cells is difficult or impractical, such as building windows/facades, vehicles, electronic device displays, etc. The main principle of TPVs is to transmit a part of the incident light in the visible band that human eyes can detect. In terms of visible light absorption, TPV technologies are classified as either wavelength-selective or non-wavelength-selective. In the wavelength-selective approach, a photoactive material is embedded in a transparent polymer substrate to absorb ultraviolet (UV) and near-infrared (NIR) light while selectively transmitting visible light. The emitted light from photoactive material is transferred to opaque PVs placed at the edge of the transparent substrate. Despite their high average visible transmittance values of 50-90%, the photovoltaic conversion efficiencies reported so far are lower than 2% [67]. In the non-wavelength-selective approach, light in the visible region is partially transmitted by either segmenting an opaque PV cell or using an ultra-thin light-absorption layer. The thin film material of TPVs can be organic, inorganic, and perovskite-based. Among them, perovskite-based thin-film TPVs achieved the highest conversion efficiency, up to 12.6% at an average visible transmittance of 21.5% [68]. Although

organic and perovskite thin film TPVs possess relatively high conversion efficiencies, they are not long-term stable because of low stability to water and oxygen. Also, they exhibit distinct colors depending on the polymers or dyes applied. Overall, there is still no perfect approach to developing TPVs with neutral color, high conversion efficiency, and long-term stability.

Crystalline silicon-based TPVs are emerging as a promising approach for developing neutral-colored, high efficient, and long-term stable transparent solar cells. Although the c-Si wafer itself is opaque, transparent c-Si substrates can be produced by drilling 3D microhole structures in the c-Si wafer. The light is transmitted through the microholes providing visible transparency independent of c-Si substrate thickness. A few studies have reported Si-based TPVs by fabricating hole arrays using conventional fabrication methods (i.e photolithography followed by DRIE) [69, 70].

For the 3D microhole arrays fabrication inside the c-Si wafer, the approach reported by Tokel, Pavlov, et al. [23] was followed, but unlike the circular motion of the laser, the sample was moved along the laser propagation direction, also the sample polishing for access to the modified regions was not needed in our study.

Here, we demonstrate the neutral-colored transparent c-Si substrate by fabricating specially designed hexagonal arrayed microholes inside the c-Si wafer using our novel ns-laser 3D structuring technique coupled with Cu-ACE. In addition to TPV applications, our work can also be applied in the fabrication of various transparent electronics.

4.2 Design Criteria for Microhole-based Transparent c-Si Substrate

Transmission in the visible light spectrum detectable by the human eye is essential for providing transparency to the Si substrate. Accordingly, the diameter (d) of the microhole needs to be designed to transmit a broad range of visible light with minimum interactions with the hole. Furthermore, the spacing (s) between the

microholes needs to be designed in a way that the human eye cannot distinguish, taking into account the minimum angle of resolution for the human eye.

4.2.1 Spacing Criterion

The spacing between the microholes is a critical factor for establishing the indistinguishability of the hole pattern. Rayleigh's criterion gives a relevant statement for our microhole-based transparent c-Si Substrate. According to the Rayleigh criterion, two separate light sources are resolved when the angle between them, θ_R, satisfies $\sin\theta_R=1.22\lambda/D$, where λ is the wavelength of the light and D is the diameter of the aperture. From this definition, the angular resolution or spatial resolution of the human eye can be estimated.

The human eye is most sensitive to green light of wavelength 555 nm [71]. The eye pupil diameter is around 4 mm, although it can vary from 2 mm in a brightly lit place to 8 mm in the dark [72]. Using the small angle approximation, the minimum angular resolution of the human eye can be calculated as follows:

$$\sin\theta_R \cong \theta_R = 1.22\frac{\lambda}{D}rad = 1.22\frac{555\ nm}{4\times10^6\ nm}rad \cong 0.00017\ rad \tag{4.1}$$

For the invisible hole pattern, the spacing (s) between the holes needs to be determined by considering the minimum angular resolution of the human eye, as shown in Figure 4.1.

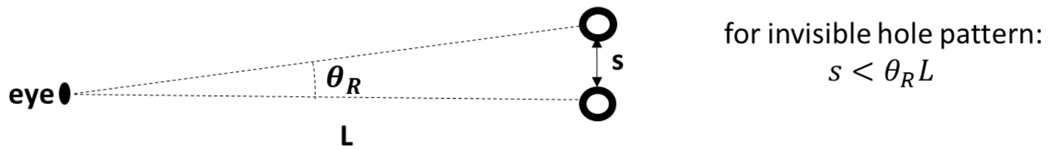

Figure 4.1 Illustration of minumum resolvable spacing between holes distinguishable by human eye at distance L from c-Si substrate.

Since L>>s, from the small angle approximation, the spacing criterion for the indistinguishable hole pattern can be expressed as, $s<\theta_R L$. At a distance of 30 cm

from the c-Si substrate (appropriate distance for reading or using mobile devices), the hole pattern will be invisible if the s<51 μm.

4.2.2 Hole Diameter Criterion

Light-hole interactions should be minimized in order to reduce haziness and hence increase the visual clarity of the transparent c-Si substrate. For this, the hole diameter should be designed to transmit a broad range of visible light with minimum optical effects (i.e., diffraction or interference). Figure 4.2 shows the simulated diffraction behavior of the visible light when interacting with c-Si periodic hole structures. The simulations were carried out in 2D using RSoft Photonic Device Tools. The spacing between the holes was chosen 20 μm for each different hole size and as a representative wavelength, 555 nm of light was chosen to propagate from bottom to top along the z-axis. For 0.5 μm hole size, there is no light transmission, whereas the transmitted light increases as the size of the holes increases. For 5 μm and 20 μm hole sizes, no clear diffractive behavior is observed since there is no considerable change in wavefronts, indicating that the behavior of the light before and after passing through the holes is the same.

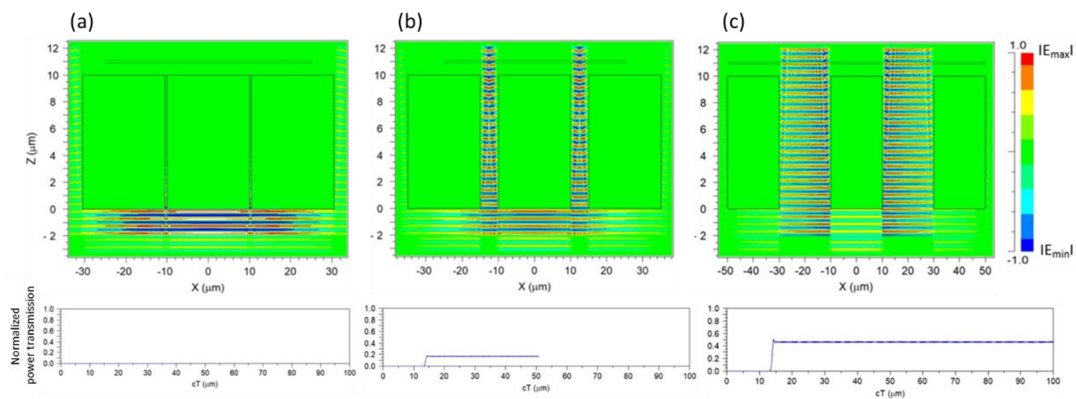

Figure 4.2 Visible light interaction with periodic holes having diameters (a) 0.5 μm, (b) 5 μm and (c) 20 μm simulated in RSoft Photonic Device Tools.

In accordance with these design considerations for spacing and hole diameter, the neutral-colored microhole-based transparent c-Si Substrate will be fabricated.

4.3 Experimental

4.3.1 Laser Subsurface Processing

First, the laser was focused on the Si surface at maximum intensity. Next, the translation stage was shifted so that the laser focus fell behind the sample. For subsurface processing, the 3D translation stage was moved back and forth perpendicular to the laser propagation direction across the entire thickness of the wafer with a scanning speed of 5 mm/s. As a result, the focused beam induced cylindrical 3D modification inside the Si sample throughout its whole thickness. For the maximum density of microholes, the Si samples were processed in a hexagonal array pattern, as illustrated in Figure 4.3.

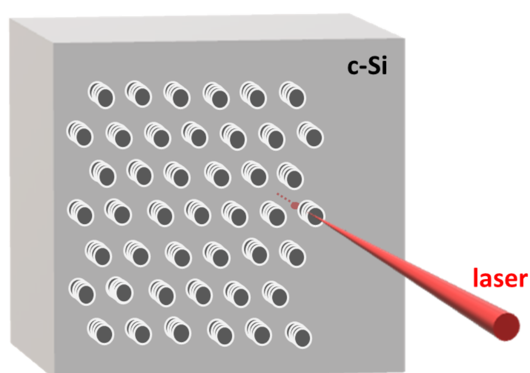

Figure 4.3 Schematic representation of subsurface processing for hexagonal arrayed microholes in c-Si substrate.

The laser was operated at a repetition rate of 100 kHz with an average output power of 2 W which corresponds to a pulse energy of 20 μJ. The intensity at the focal point was calculated to be ~5.6 GW/cm^2 and this value was sufficient to produce subsurface modification inside the Si wafer for microhole fabrication.

4.3.2 Fabrication Procedure of Microhole-based Transparent c-Si Substrate

Double-side polished, 280 µm thick, single-crystalline p-type Si wafer with <100> orientation and 1-3 Ω.cm resistivity were used in the fabrication of transparent c-Si substrate. Hexagonal arrayed microholes were prepared in 8 mm × 8 mm process areas with 60 µm, 70 µm, and 80 µm periods (center-to-center distance of the holes). Number of holes and laser process times are shown for each period in Table 4.1. After laser structuring, the Si substrate was cleaned in a DI water ultrasonic bath for 5 minutes to remove the silicon dust around the modified regions. The diameter of the laser-modified cylindrical regions were measuered around 21 µm for each different period, as seen in optical microscope images in Figure 4.4.

Table 4.1 Number of holes and laser process times for hexagonal arrayed microholes with different periods. (Process area: 8 mm × 8 mm).

Period (µm)	Hole number	Laser process time (hr:min)
60	133×133	05:32
70	114×114	04:00
80	100×100	03:07

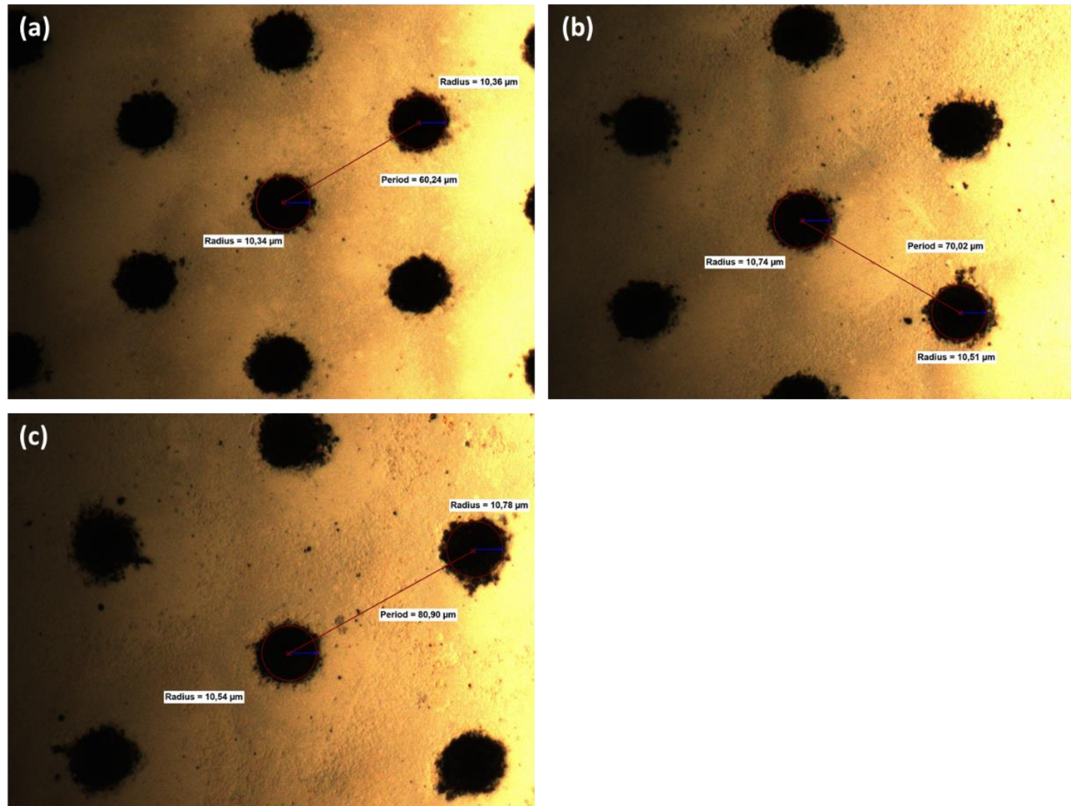

Figure 4.4 Optical microscope images showing diameters of laser-modified regions for (a) 60 µm (b) 70 µm and (c) 80 µm periods.

The laser-modified parts were etched in the highly selective Cu-ACE solution. The sufficient etching time was around 45-50 minutes to reveal 3D hole structures out of the Si bulk. For etching, 100 ml of Cu-ACE solution was used. The c-Si wafer was cleaned in diluted HF for about 30 seconds before and after etching and rinsed with DI water. Figures 4.5, 4.6, and 4.7 show SEM images of etched microholes having 60 µm, 70 µm, and 80 µm hole periods, respectively. Microhole structures having the 60 µm period almost disappeared as seen in Figure 4.5. The diameter of the microholes was measured at around 63 µm for both 70 µm and 80 µm periods as shown in Figures 4.6 (c) and 4.7 (c). And, the spacings were measured at 7 µm and 17 µm for the 70 µm and 80 µm hole periods, respectively, which are lower than the spacing criterion for the invisible hole pattern. However, from cross-section images 4.6 (b) and (d), it can be seen that some parts of lateral surfaces of the microholes were totally etched for the 70 µm period. Nevertheless, we demonstrated that nearly

perfect circular microholes having smooth surfaces can be produced with our two-step fabrication. The etching time was determined according to complete etching of the laser-modified region within the Si wafer throughout its entire thickness. In this regard, we fabricated microholes with controlled spacing but with a maximum diameter of 63 µm. Extending the etching time to increase the hole diameter was not prefered as it can deteriorate the surface.

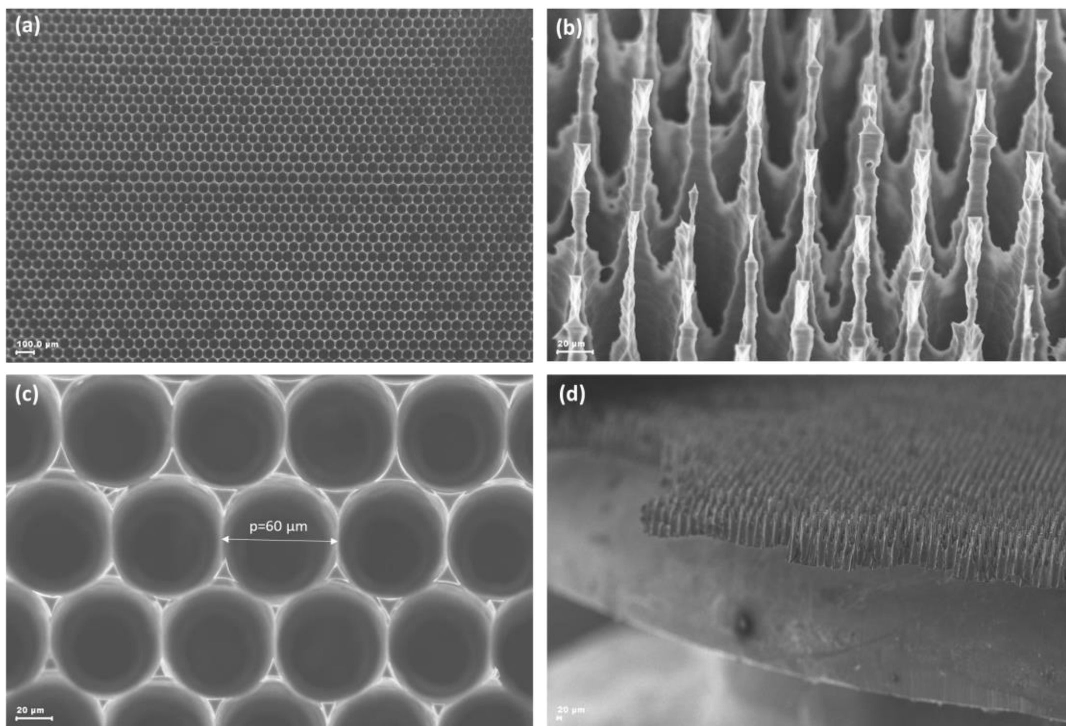

Figure 4.5 SEM images of etched Si microhole arrays having 60 µm period. (a) Top surface image at 100X magnification, (b) 75^0 tilted image at 1000X magnification, (c) top surface image at 1000X magnification, (d) 75^0 tilted cross-section image at 100X magnification.

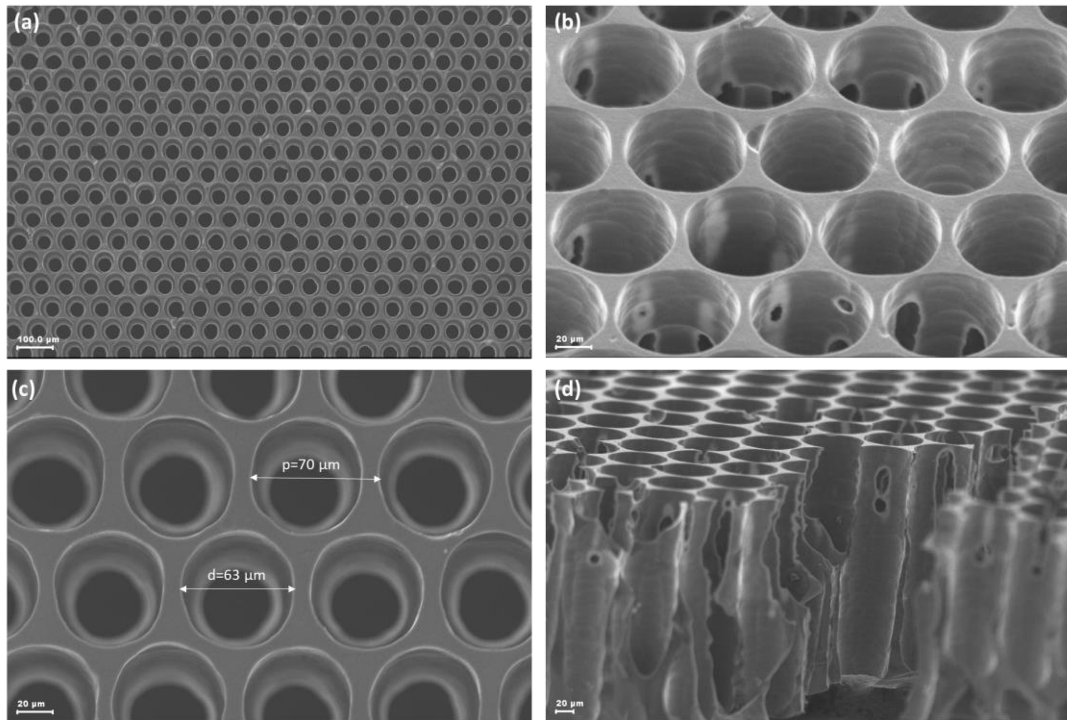

Figure 4.6 SEM images of etched Si microhole arrays having 70 μm period. (a) Top surface image at 200X magnification, (b) 75^0 tilted image at 1000X magnification, (c) top surface image at 1000X magnification, (d) 75^0 tilted cross-section image at 500X magnification.

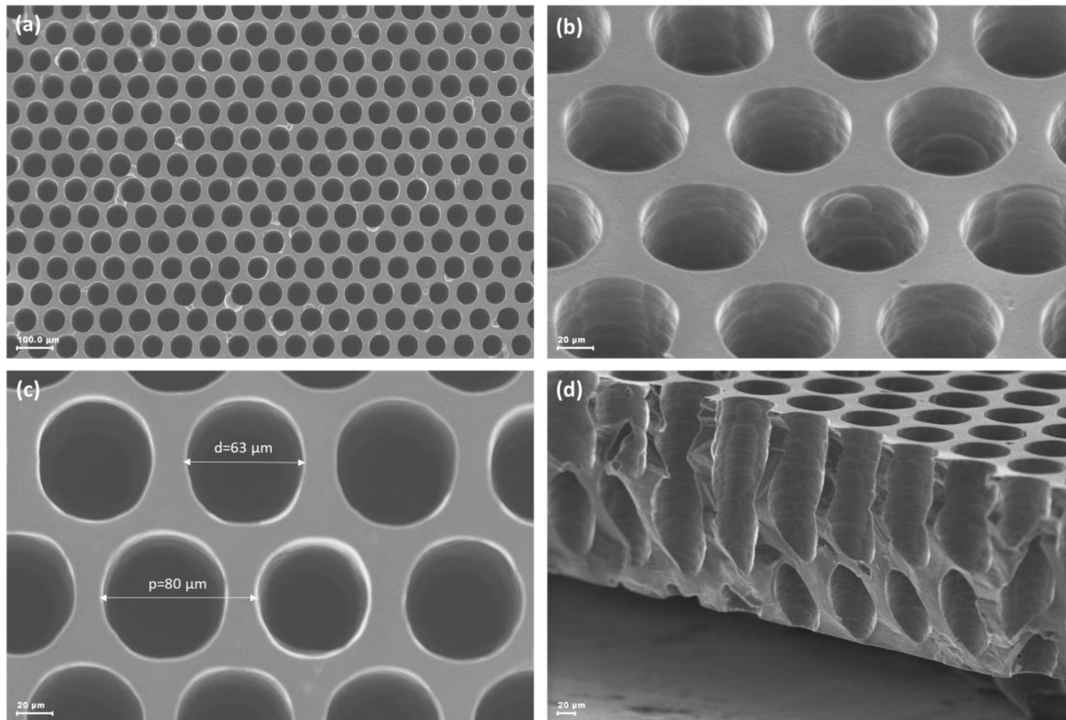

Figure 4.7 SEM images of etched Si microhole arrays having 80 μm period. (a) Top surface image at 200X magnification, (b) 75^0 tilted image at 1000X magnification, (c) top surface image at 1000X magnification, (d) 75^0 tilted cross-section image at 500X magnification

Figure 4.8 (a) shows measured transmittance spectrums of the hexagonal arrayed c-Si microholes with different periods and photographs in Figure 4.8 (b) show the fabricated neutral-colored transparent c-Si substrate that has different hole periods in each transparent region. It can be seen that the transmittance values are almost the same in the visible wavelength region, confirming the neutral color of the c-Si substrate.

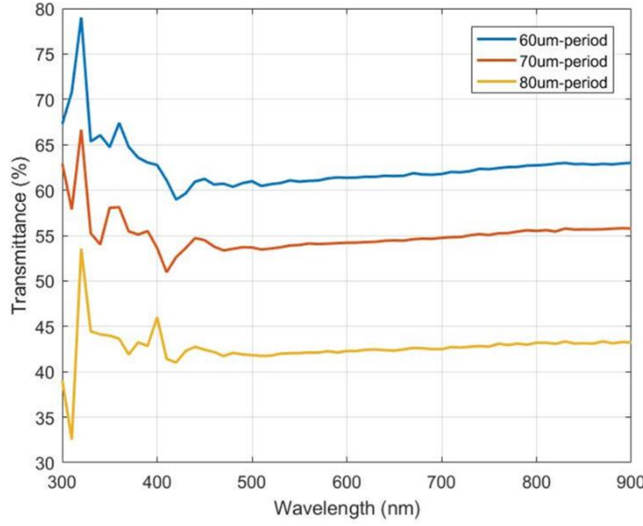

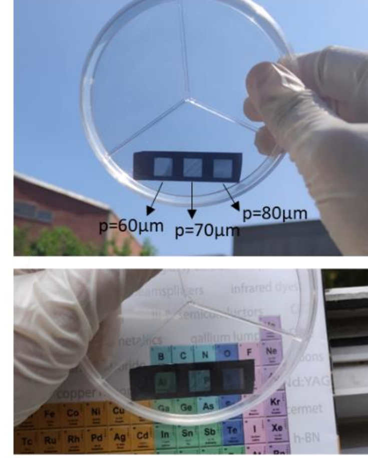

(a) (b)

Figure 4.8 (a) Transmittance spectra of hexagonal arrayed c-Si microholes with different periods. (b) Corresponding neutral-colored transparent c-Si substrate where each transparent region having a different hole period as indicated in upper photograph.

4.3.2.1 Average Visible Transmittance and Color Rendering

The recommended approach to evaluate the transparency level of TPVs is based on the average visible transmittance (AVT) considering not only the transmittance spectrum (T) of the sample but also the spectral sensitivity of the human eye through the photopic response (P) and the solar spectral irradiance (S) in AM1.5G conditions. In general, AVT is calculated in the visible wavelength range (380-780 nm) as follows [67, 73, 74]:

$$AVT = \frac{\int T(\lambda)P(\lambda)S(\lambda)d(\lambda)}{\int P(\lambda)S(\lambda)d(\lambda)} \tag{4.2}$$

Equation 4.2 yields the AVT values of 42.1%, 53.9%, and 60.9% for the transparent regions on the c-Si substrate having 80 µm, 70 µm, and 60 µm hole periods, respectively. The AVT values and associated filling fraction values are given in Table 4.2. The filling fraction which is the ratio of the light absorption region to the

entire process region provides control of the transmittance. As expected, the highest filling fraction value was obtained at the lowest AVT value, due to increased spacing value for the light absorption region.

Table 4.2 Filling fraction and AVT values at different hole diameters and spacings.

Period (µm)	Diameter (µm)	Spacing (µm)	Filling Fraction (%)	AVT (%)
60	60	0	21.5	60.9
70	63	7	36.4	53.9
80	63	17	51.3	42.1

The CIE 1931 chromaticity diagram is a graphical representation of all colors perceived by the human eye [75]. The chromaticity (color) coordinates of any point on the diagram are labeled x and y and describe the saturation of light. The CIE 1931 chromaticity diagram was used to provide a quantitative measure of the color perception of the fabricated transparent c-Si substrate. The chromaticity coordinates with respect to the transmittance spectra of the c-Si substrate were computed and imposed in the CIE 1931 color space diagram [76]. Figure 4.9 shows the corresponding color coordinates of the transparent regions on the c-Si substrate with different hole periods on the CIE 1931 chromaticity diagram. The CIE standard illuminant D65 representing natural daylight is also added to the diagram. Monochromatic colors are positioned on the perimeter of the diagram and the saturation of the colors reduces towards the center (i.e. white region). As seen in the diagram, the color coordinates of the transparent c-Si substrate are located in the white region close to the standard daylight illuminant D65. Thus, the color coordinates suggest neutral color (achromatic) transparency for our transparent c-Si substrate.

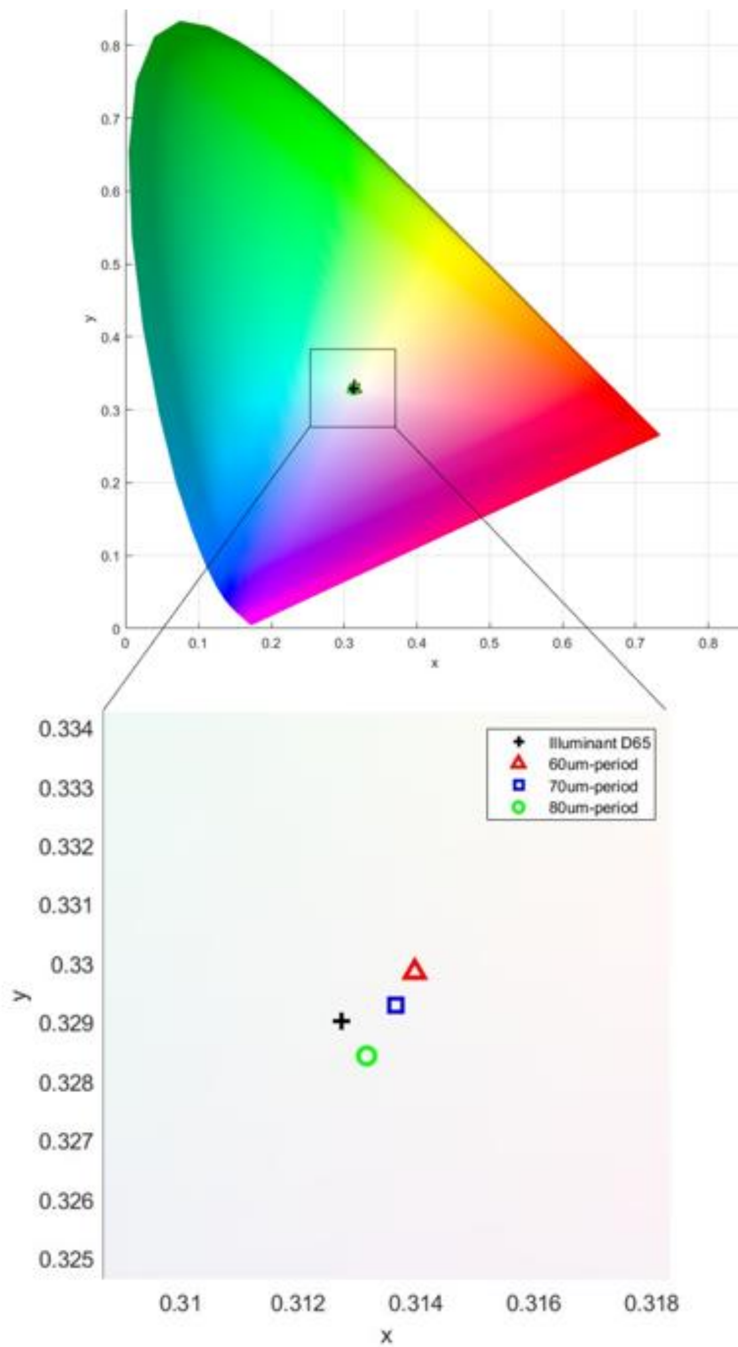

Figure 4.9 CIE 1931 chromaticity diagram showing color coordinates of the transparent regions on the c-Si substrate having different hole periods. (Illuminant D65 represents color coordinates of standard daylight illuminant.)

4.3.2.2 Square Arrayed c-Si Microholes

Square arrayed microholes with 80 μm period were prepared on 10 mm × 10 mm process area. Figure 4.10 (a) is the optical microscope image showing the laser-modified cylindrical regions with a diameter of around 21 μm. Following the same fabrication technique as the hexagonal arrayed microholes, after the etching step, the diameter of the square arrayed microholes was measured at around 61 μm, as seen top view SEM image in Figure 4.10 (b). In order to obtain cross-section view, the sample was carefully cut, and the cross-sectional area was polished to reveal the cylindrical shape of the holes. As seen from Figure 4.10 (c), the microholes are in cylindrical shape since the hole diameters are almost the same on the top and bottom surfaces. The reason for the increase in hole diameter seen in the cross-sectional SEM image is that the sample is cleaned with Piranha solution for 40 minutes after polishing.

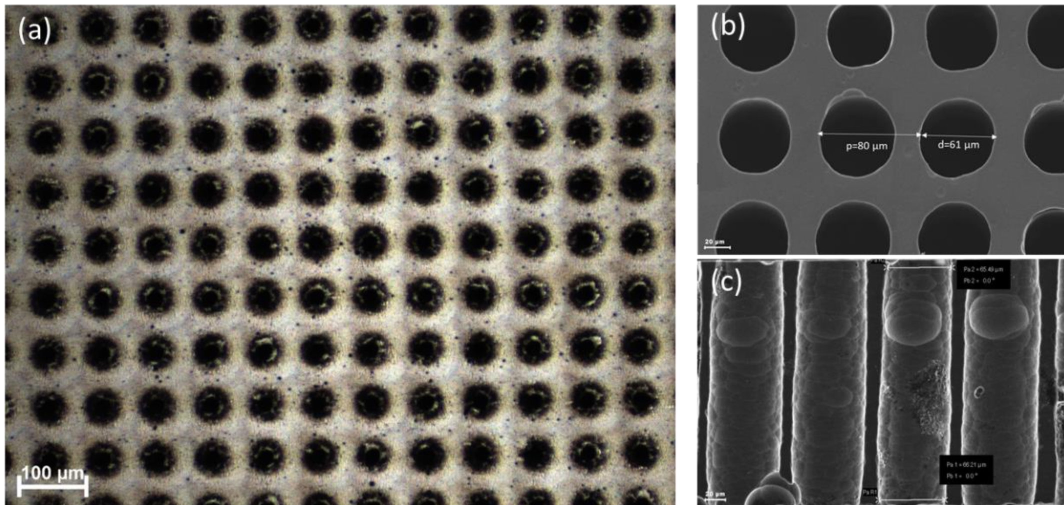

Figure 4.10 (a) Optical microscope images of laser-modified square arrayed region. (b) Top view SEM image of etched Si microhole arrays having 80 μm period at 1000X magnification. (c) Cross-section SEM image of etched and polished Si microhole arrays at 800X magnification.

Figure 4.11 (a) shows measured transmittance spectrums of the square arrayed c-Si microholes. In Figure 4.11 (b), the top left photo of the laser-structured sample was taken before etching, and the other two photos were taken after etching. The AVT

value of 41.5% was calculated from Equation 4.2 in the visible wavelength range (380-780 nm). The number of microholes on the 10 mm × 10 mm process area was 125 × 125, giving a filling fraction value of 54.3%. The chromaticity coordinates of the c-Si substrate in the CIE 1931 color space diagram were found as (x=0.3132, y=0.3297), which is again located in the white region confirming the neutral color transparency of the substrate.

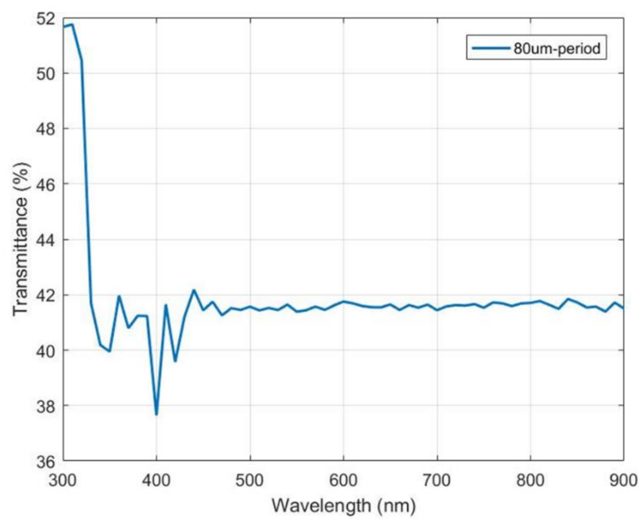

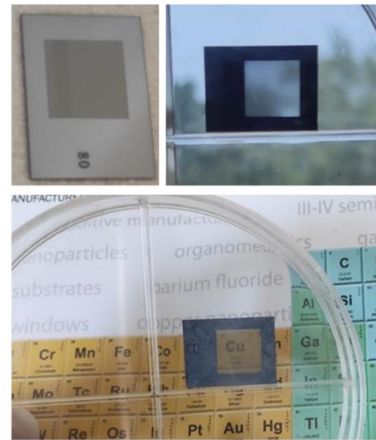

(a) (b)

Figure 4.11 (a) Transmittance spectra of square arrayed c-Si microholes with 80 μm period. (b) Corresponding neutral-colored transparent c-Si substrate. (Upper left photo is of laser-structured c-Si substrate taken before etching.)

CHAPTER 5

CONCLUSION

In this thesis, highly controllable laser-induced surface and subsurface modifications in c-Si have been demonstrated without damaging the surface by using a custom-built nanosecond pulsed infrared laser. Highly selective etching of the laser-modified region to reveal 3D structures out of the c-Si bulk was accomplished by utilizing the Cu-ACE solution. Our novel maskless two-step approach has been successfully applied to produce 3D microhole arrays inside the c-Si wafer, and 3D micropillar arrays on the surface of the c-Si wafer. The method demonstrated here is low-cost, involves fewer processing steps than traditional lithographic methods, and is scalable to large areas, thus can be easily adjusted to different applications.

In Chapter 3, optimum pillar dimensions with good-quality c-Si surface were determined for potential application in c-Si micropillar array solar cells. The highest quality periodic 3D micropillar arrays with 17.46% surface reflectance were fabricated on the c-Si wafer for 20 μm laser step-sized micropillar structures with 13.5±1 μm width and 17±1 μm length. The dimensions of the fabricated pillar structures were suitable for the radial pn junction formation. Also, the contamination of Cu particles on the c-Si micropillar surface was prevented by the cleaning procedure applied after Cu-ACE. Therefore, in a proper clean room environment with specialized equipment for the etching, our study of the c-Si micropillar arrays can be continued to fabricate the radial junction solar cell.

In Chapter 4, we report the first demonstration of the neutral-colored transparent c-Si substrate fabricated by using ns-laser 3D subsurface structuring technique coupled with Cu-ACE. Specially designed hexagonal and square arrayed microholes inside the c-Si wafers were generated to provide transparency to the substrate. And, nearly perfect circular microholes having smooth surfaces were produced through 280 μm

thick c-Si wafer with our novel two-step fabrication. To evaluate the transparency level of the substrate quantitatively, first transmittance spectrums were measured, and then AVT values and chromaticity coordinates were calculated in the visible wavelength range in accordance with the transmittance spectra and spectral sensitivity of the human eye (photopic response). The microhole arrays were fabricated with controlled AVT values between 40% and 60% by varying the hole periods. High AVT values have indicated the transparency of the c-Si substrate, while the color space coordinates have confirmed the neutral color transparency of our transparent c-Si substrate. The use of c-Si in TPVs has emerged as a promising approach due to its high efficiency and long-term stability. And, since our fabrication method for the neutral-colored transparent c-Si substrate is rapid and low-cost, it holds great potential for the TPV industry.

REFERENCES

1. Einstein, A., Zur Quantentheorie der Strahlung. Physikalische Zeitschrift, 1917. 18: p. 121-128.

2. Maiman, T.H., Stimulated Optical Radiation in Ruby. Nature, 1960. 187(4736): p. 493-494.

3. Schaaf, P., Laser Processing of Materials: Fundamentals, Applications and Developments. Vol. 139. 2010.

4. Meijer, J., et al., Laser Machining by short and ultrashort pulses, state of the art and new opportunities in the age of the photons. CIRP Annals, 2002. 51(2): p. 531-550.

5. Prakash, S. and S. Kumar, 6 - Microchannel fabrication via direct laser writing, in Microfabrication and Precision Engineering, J.P. Davim, Editor. 2017, Woodhead Publishing. p. 163-187.

6. Dahotre, N.B. and S. Harimkar, Laser fabrication and machining of materials. 2008: Springer Science & Business Media.

7. Sugioka, K. and Y. Cheng, A tutorial on optics for ultrafast laser materials processing: basic microprocessing system to beam shaping and advanced focusing methods. Advanced Optical Technologies, 2012. 1(5): p. 353-364.

8. Chambonneau, M., et al., In-Volume Laser Direct Writing of Silicon—Challenges and Opportunities. Laser & Photonics Review, 2021. 15: p. 1–35.

9. Gamaly, E.G. and A.V. Rode, Physics of ultra-short laser interaction with matter: From phonon excitation to ultimate transformations. Progress in Quantum Electronics, 2013. 37(5): p. 215-323.

10. Gattass, R. and E. Mazur, Femtosecond Laser Micromachining in Transparent Materials. Nature Photonics, 2008. 2: p. 219-225.

11. Jalali, B. and S. Fathpour, Silicon Photonics. Lightwave Technology, Journal of, 2007. 24: p. 4600-4615.

12. Vorobyev, A. and C. Guo, Laser turns silicon superwicking. Optics express, 2010. 18: p. 6455-60.

13. Vorobyev, A. and C. Guo, Direct creation of black silicon using femtosecond laser pulses. Applied Surface Science - APPL SURF SCI, 2011. 257: p. 7291-7294.

14. Nejadmalayeri, A.H., et al., Inscription of optical waveguides in crystalline silicon by mid-infrared femtosecond laser pulses. Optics letters, 2005. 30 9: p. 964-6.

15. Grojo, D., et al., Limitations to laser machining of silicon using femtosecond micro-Bessel beams in the infrared. Journal of Applied Physics, 2015. 117(15): p. 153105.

16. Kononenko, V., V. Konov, and E. Dianov, Delocalization of femtosecond radiation in silicon. Optics letters, 2012. 37: p. 3369-71.

17. Tokel, O., et al., Laser-Writing in Silicon for 3D Information Processing. 2014.

18. Pavlov, I., et al., Diffraction-limited, 10-W, 5-ns, 100-kHz, all-fiber laser at 155 μm. Optics letters, 2014. 39: p. 2695-2698.

19. Pavlov, I., et al., Femtosecond laser written waveguides deep inside silicon. Optics Letters, 2017. 42(15): p. 3028-3031.

20. Yu, X., et al., Internal modification of intrinsic and doped silicon using infrared nanosecond laser. Applied Physics A, 2016. 122(12): p. 1001.

21. O'Neill, W. and K. Li, High-Quality Micromachining of Silicon at 1064 nm Using a High-Brightness MOPA-Based 20-W Yb Fiber Laser. Selected Topics in Quantum Electronics, IEEE Journal of, 2009. 15: p. 462-470.

22. Richardson, D.J., J. Nilsson, and W.A. Clarkson, High power fiber lasers: current status and future perspectives [Invited]. Journal of the Optical Society of America B, 2010. 27(11): p. B63-B92.

23. Tokel, O., et al., In-chip microstructures and photonic devices fabricated by nonlinear laser lithography deep inside silicon. Nature Photonics, 2017. 11(10): p. 639-645.

24. Hasselbeck, M.P., NONLINEAR OPTICS, BASICS | Nomenclature and Units, in Encyclopedia of Modern Optics, R.D. Guenther, Editor. 2005, Elsevier: Oxford. p. 240-246.

25. Liu, Q., X. Duan, and C. Peng, Laser Micro-/Nanofabrication and Applications Based on Multiphoton Process, in Novel Optical Technologies

for Nanofabrication, Q. Liu, X. Duan, and C. Peng, Editors. 2014, Springer Berlin Heidelberg: Berlin, Heidelberg. p. 81-151.

26. Trebino, R. and J. Buck, 4. Nonlinear Optics. 2000.

27. Boyd, R., Preface to the Third Edition, in Nonlinear Optics (Third Edition), R.W. Boyd, Editor. 2008, Academic Press: Burlington. p. xiii-xiv.

28. Leuthold, J., C. Koos, and W. Freude, Nonlinear Silicon Photonics. Nature Photonics, 2010. 4: p. 535-544.

29. Tsang, H., et al., Optical dispersion, two-photon absorption and self-phase modulation in silicon waveguides at 1.5 μm wavelength. Applied Physics Letters, 2002. 80: p. 416-418.

30. Gamaly, E., Femtosecond laser-matter interaction: Theory, experiments and applications. Femtosecond Laser-Matter Interaction: Theory, Experiments and Applications, 2011.

31. Gamaly, E., et al., Laser-matter interaction in the bulk of a transparent solid: Confined microexplosion and void formation. Physical Review B, 2006. 7350.

32. Majumdar, J. and I. Manna, Laser-Assisted Fabrication of Materials. Vol. 161. 2013.

33. Laermer, F. and A. Schilp, Method of anisotropic etching of silicon. 2003, U.S. Patent 6,531,068 B2.

34. Wu, B., A. Kumar, and S. Pamarthy, High aspect ratio silicon etch: A review. Journal of Applied Physics, 2010. 108(5): p. 051101.

35. Huang, Z., et al., Metal-Assisted Chemical Etching of Silicon: A Review. Advanced materials (Deerfield Beach, Fla.), 2011. 23: p. 285-308.

36. Choi, H.-J., et al., Optimization of metal-assisted chemical etching process in fabrication of p-type silicon wire arrays. Current Applied Physics, 2011. 11: p. S25–S29.

37. Leonardi, A., M.J. Lo faro, and A. Irrera, Silicon Nanowires Synthesis by Metal-Assisted Chemical Etching: A Review. Nanomaterials, 2021. 11: p. 383.

38. Um, H.-D., et al., Versatile control of metal-assisted chemical etching for vertical silicon microwire arrays and their photovoltaic applications. Scientific Reports, 2015. 5(1): p. 11277.

39. Kong, L., et al., Evidences for redox reaction driven charge transfer and mass transport in metal-assisted chemical etching of silicon. Scientific Reports, 2016. 6.

40. Wilhelm, T., et al., Fabrication of Suspended III–V Nanofoils by Inverse Metal-Assisted Chemical Etching of In 0.49 Ga 0.51 P/GaAs Heteroepitaxial Films. ACS Applied Materials & Interfaces, 2018. 10.

41. Han, H., Z. Huang, and W. Lee, Metal-assisted chemical etching of silicon and nanotechnology applications. Nano Today, 2014. 9(3): p. 271-304.

42. Li, X., Metal assisted chemical etching for high aspect ratio nanostructures: A review of characteristics and applications in photovoltaics. Current Opinion in Solid State and Materials Science, 2012. 16(2): p. 71-81.

43. Li, X. and P.W. Bohn, Metal-assisted chemical etching in HF/H2O2 produces porous silicon. Applied Physics Letters, 2000. 77(16): p. 2572-2574.

44. Hildreth, O., W. Lin, and C.P. Wong, Effect of Catalyst Shape and Etchant Composition on Etching Direction in Metal-Assisted Chemical Etching of Silicon to Fabricate 3D Nanostructures. ACS nano, 2009. 3: p. 4033-42.

45. Peng, K.-Q., et al., Fabrication of Single-Crystalline Silicon Nanowires by Scratching a Silicon Surface with Catalytic Metal Particles. Advanced Functional Materials, 2005. 16: p. 387-394.

46. Chartier, C., S. Bastide, and C. Lévy-Clément, Metal-assisted chemical etching of silicon in HF–H2O2. Electrochimica Acta, 2008. 53(17): p. 5509-5516.

47. Koynov, S., M.S. Brandt, and M. Stutzmann, Black nonreflecting silicon surfaces for solar cells. Applied Physics Letters, 2006. 88(20): p. 203107.

48. Leng, X., C. Wang, and Z. Yuan, Progress in metal-assisted chemical etching of silicon nanostructures. Procedia CIRP, 2020. 89: p. 26-32.

49. Kim, J., et al., Au/Ag Bilayered Metal Mesh as a Si Etching Catalyst for Controlled Fabrication of Si Nanowires. ACS nano, 2011. 5: p. 3222-9.

50. Kuo, K.-H., W.-H. Ku, and B. Lee, Photoluminescent or Blackened Silicon Surfaces Synthesized with Copper-assisted Chemical Etching: For Energy Applications. ECS Journal of Solid State Science and Technology, 2020. 9: p. 024006.

51. Chandler, T.C., MEMC Etch—A Chromium Trioxide-Free Etchant for Delineating Dislocations and Slip in Silicon. Journal of The Electrochemical Society, 1990. 137(3): p. 944-948.

52. Morinaga, H., M. Suyama, and T. Ohmi, Mechanism of Metallic Particle Growth and Metal-Induced Pitting on Si Wafer Surface in Wet Chemical Processing. Journal of The Electrochemical Society, 1994. 141(10): p. 2834-2841.

53. Williams, M.O., M. Kolhep, and M. Zacharias, Effect of Various Copper Salt Precursors on Metal-Assisted Chemical Etching of Silicon. ECS Journal of Solid State Science and Technology, 2019. 8(2): p. P93-P98.

54. Wang, Y., et al., Micro-structured inverted pyramid texturization of Si inspired by self-assembled Cu nanoparticles. Nanoscale, 2016. 9.

55. Kolasinski, K., Metal Assisted Catalytic Etching (MACE) for Nanofabrication of Semiconductor Powders. 2021.

56. Singh, J., Electronic and Optoelectronic Properties of Semiconductor Structures. 2003, Cambridge: Cambridge University Press.

57. Kelzenberg, M.D., et al., Enhanced absorption and carrier collection in Si wire arrays for photovoltaic applications. Nature Materials, 2010. 9(3): p. 239-244.

58. Yoon, H., et al., Enhanced conversion efficiencies for pillar array solar cells fabricated from crystalline silicon with short minority carrier diffusion lengths. Applied Physics Letters, 2010. 96: p. 213503-213503.

59. Hwang, I., et al., Flexible crystalline silicon radial junction photovoltaics with vertically aligned tapered microwires. Energy & Environmental Science, 2018. 11.

60. Yablonovitch, E., Statistical ray optics. Journal of the Optical Society of America, 1982. 72(7): p. 899-907.

61. Kayes, B., H. Atwater, and N. Lewis, Comparison of the device physics principles of planar and radial p-n junction nanorod solar cells. Journal of Applied Physics, 2005. 97: p. 114302-114302.

62. Lee, K., et al., 17.6%-Efficient radial junction solar cells using silicon nano/micro hybrid structures. Nanoscale, 2016. 8.

63. Um, H.-D., et al., Progress on Silicon Microwire Solar Cells. Journal of Materials Chemistry A, 2020. 8.

64. Alaeian, H., A. Atre, and J. Dionne, Optimized light absorption in Si wire array solar cells. Journal of Optics, 2012. 14.

65. Kosten, E., E. Warren, and H. Atwater, Ray optical light trapping in silicon microwires: Exceeding the 2n2 intensity limit. Optics express, 2011. 19: p. 3316-31.

66. Internatonal, A. ASTM G173-03 (2012)-Standard Tables for Reference Solar Spectral Irradiances: Direct Normal and Hemispherical on 37◦ Tilted Surface. in ASTM. 2012.

67. Traverse, C.J., et al., Emergence of highly transparent photovoltaics for distributed applications. Nature Energy, 2017. 2: p. 849-860.

68. Lee, K., et al., The Development of Transparent Photovoltaics. Cell Reports Physical Science, 2020. 1(8): p. 100143.

69. Kang, S.B., et al., Colorful Transparent Silicon Photovoltaics with Unprecedented Flexibility. Advanced Functional Materials, 2022. 32.

70. Lee, K., et al., Neutral-Colored Transparent Crystalline Silicon Photovoltaics. Joule, 2020. 4(1): p. 235-246.

71. Gross, H., Handbook of Optical Systems. 2008. 1-826.

72. Hecht, E. and A. Zajac, Optics. 2 ed. 1987: Addison-Wesley.

73. Glass in building Determination of light transmittance, solar direct transmittance, total solar energy transmittance, ultraviolet transmittance and related glazing factors (ISO 9050:2003).

74. CIE standard colorimetric observers (ISO 10527:1991).

75. International Commission on Illumination. [Online]. Available from: cie.co.at.

76. Tingbiao Guo, Convert spectrum to color 2022; Available from: https://www.mathworks.com/matlabcentral/fileexchange/98289-convert-spectrum-to-color.